

## Tailored PDFs for New Physics searches

---

**Ella Cole<sup>a</sup> , Mark N. Costantini<sup>a</sup> , Elie Hammou<sup>b</sup> , Luca Mantani<sup>c</sup> ,  
Francesco Merlotti<sup>d</sup> , Manuel Morales-Alvarado<sup>e</sup> and Maria Ubiali<sup>a</sup>**

<sup>a</sup>*DAMTP, University of Cambridge, Wilberforce Road, Cambridge, CB3 0WA, United Kingdom*

<sup>b</sup>*Nikhef Theory Group, Science Park 105, 1098 XG Amsterdam, The Netherlands*

<sup>c</sup>*Instituto de Física Corpuscular (IFIC), Universidad de Valencia-CSIC, E-46980 Valencia, Spain*

<sup>d</sup>*Institute for Theoretical Physics, ETH, Wolfgang-Pauli-Strasse 27, CH-8093 Zürich, Switzerland*

<sup>e</sup>*INFN, Sezione di Trieste, SISSA, Via Bonomea 265, 34136, Trieste, Italy*

*E-mail:* [ehammou@nikhef.nl](mailto:ehammou@nikhef.nl), [m.ubiali@damtp.cam.ac.uk](mailto:m.ubiali@damtp.cam.ac.uk)

**ABSTRACT:** Given the non-negligible interplay between parton distribution functions (PDFs) at large  $x$  and potential New Physics (NP) effects in the high-energy tails of hadron collider observables, a central question is which PDFs can be reliably employed in beyond-the-Standard-Model (BSM) analyses. In this work, we examine the fine balance between using PDF sets with small uncertainties in the large- $x$  region – crucial for maximising BSM sensitivity – and adopting conservative PDF fits that exclude high-energy data potentially contaminated by unaccounted NP contributions. We systematically assess a range of conservative PDF fitting strategies designed to mitigate such biases and provide a recommendation for the class of PDFs best suited for robust BSM searches. In addition, we investigate the alternative approach of performing simultaneous fits of Standard Model Effective Field Theory (SMEFT) Wilson coefficients and PDFs, thereby consistently accounting for their mutual correlations. Starting from a toy model to illustrate the underlying mechanisms, we then analyse two realistic NP scenarios: one modifying high-mass Drell–Yan production and another affecting the high-invariant-mass tail of top-quark pair production. Both cases are representative of measurements that will be probed with high precision during the High-Luminosity phase of the LHC.

**KEYWORDS:** Parton Distribution Functions, HL-LHC, BSM, SMEFT, New Physics searches

ARXIV EPRINT: [2602.xxxxx](https://arxiv.org/abs/2602.xxxxx)

---

## Contents

<b>1</b>	<b>Introduction</b>	<b>1</b>
<b>2</b>	<b>A toy model for global PDF and SMEFT fits</b>	<b>3</b>
2.1	Presentation of the model	3
2.2	Analytic derivations	6
2.3	Results	9
<b>3</b>	<b>Disentangling new physics signals and PDFs at the HL-LHC</b>	<b>11</b>
3.1	Analysis settings	11
3.2	BSM and PDF interplay in the Drell-Yan sector	15
3.3	BSM and PDF interplay in the top sector	20
<b>4</b>	<b>Practical recommendations</b>	<b>24</b>
4.1	Implementing energy cut-offs	24
4.2	Breaking Bjorken- $x$ and $M^2$ degeneracy	27
4.3	Comparing different sectors	29
<b>5</b>	<b>Conclusions</b>	<b>31</b>
<b>A</b>	<b>Description of the new physics scenarios</b>	<b>34</b>
A.1	The $W'$ model and the $\hat{W}$ parameter	34
A.2	The $Z'$ model and the $\hat{Y}$ parameter	34
A.3	The coloron model $\mathcal{G}$ and the $\hat{Z}$ parameter	35
<b>B</b>	<b>Presentation of the dataset</b>	<b>36</b>
<b>C</b>	<b>Evaluation of fit qualities</b>	<b>42</b>

---

## 1 Introduction

Over the past decade, the role of global beyond-the-Standard-Model (BSM) fits has undergone a significant evolution. Early studies were primarily focused on forecasting the discovery reach of the LHC and identifying promising channels in which new physics (NP) signals might first emerge. However, following several null results from Run-I and Run-II, the emphasis has progressively shifted towards interpreting increasingly precise Standard Model (SM) measurements in the absence of clear deviations. In this context, global analyses have moved from predominantly parameter-estimation exercises within specific BSM frameworks to more comprehensive strategies aimed at model comparison, consistency tests, and the systematic assessment of correlated uncertainties [1, 2]. This shift

has sharpened the need to understand subtle theoretical systematics—among them, the interplay between BSM effects and Parton Distribution Functions (PDFs)—which may critically impact the interpretation of high-energy collider data.

In recent years, such an interplay between PDFs and NP has been extensively investigated [3–14]. It was explicitly shown that, as experimental precision increases and more statistics are accumulated in the high-mass region at the HL-LHC, large- $x$  PDFs can mimic the effects of certain new physics scenarios. For example, a heavy  $SU(2)_L$  triplet that couples universally to all quark flavours [15] can indirectly alter the tails of Drell–Yan distributions used in PDF fits. These effects can be absorbed by the relatively unconstrained antiquark distributions at large  $x$  [11]. Similar issues might arise when considering new physics models that affect the large- $p_T$  tails of inclusive jet distributions or the large- $m_{jj}$  tails of the dijet distributions that might be absorbed by the poorly constrained large- $x$  gluon [16, 17]. Looking ahead, data from future facilities such as the Electron-Ion Collider (EIC) [18] and experiments from the Forward Physics Facilities at CERN [19] will provide complementary information to disentangle genuine new physics effects from large- $x$  PDF uncertainties [12], while lattice-QCD constraints are also expected to contribute in this direction [20].

Given the importance of this phenomenological issue, several computational frameworks have been developed to systematically assess the interplay between PDFs and new physics by enabling simultaneous fits of PDFs and BSM parameters, often within the model-independent Standard Model Effective Field Theory (SMEFT) framework. Among these, the tool `SIMUnet` allows for the simultaneous determination of PDFs and an arbitrary number of SMEFT operators, including their linear effects on observables [14]. Similarly, a version of `XFitter` [13] supports joint fits of PDFs and SMEFT operators, although the number of implemented operators is currently limited. Both tools are tightly connected to specific PDF parametrisations, NNPDF4.0 in the case of `SIMUnet`, and a polynomial-based form in the case of `XFitter`. The `Colibri` framework [21, 22] provides an even more flexible environment, which in the near future will allow for a simultaneous determination of PDFs and SMEFT parameters for any PDF parametrisation.

Despite recent progress, several open questions remain in this field, two of which we aim to address in this work.

- (i) Given that the inclusion of data probing the high-energy tails of distributions in PDF fits might be problematic, as PDFs may be able to mimic and absorb the effects of certain new physics models, should we adopt a more conservative approach by excluding all data above a given energy scale, defined by a cut-off  $Q_{\max}^2$ ?
- (ii) How to properly use the results of a joint PDF–SMEFT determination? Specifically, given the output of a simultaneous PDF–SMEFT fit, can the resulting “SMEFT PDF” be employed directly as input for precision collider predictions or indirect BSM searches? Must the assumptions underlying any subsequent analysis be consistent with those made in the joint PDF–SMEFT determination, or can such PDFs be used independently? Furthermore, could the difference between a SM-only PDF fit and a simultaneous PDF–SMEFT fit be interpreted as an estimate of the systematic

uncertainty associated with standard PDF determinations? And can a difference in the fit quality be used to conclude that there is evidence of EFT effects?

Answering these questions will be of great value not only to those pursuing precision phenomenology at the LHC but also to the broader BSM community, including experimental collaborations engaged in direct and indirect searches for new physics. In this paper, we tackle both questions. We will show that, while conservative fits may appear to be the most robust and model-independent choice, they have several drawbacks, as they rely heavily on older experimental data and on the ability of PDF-fitting frameworks to accurately handle extrapolations into poorly constrained regions.

The structure of this work is as follows. In Section 2, we present the main mathematical ideas of this work in the context of a simple toy model. Whilst this toy model is a gross simplification of the realistic phenomenological scenario we face, it presents a number of features which translate well to the numerical study we subsequently perform. In Section 3, we set the HL-LHC scenario that we aim to explore and define two BSM models that affect the Drell-Yan and the top sector respectively. We then perform a thorough phenomenological study to probe the usefulness of the ‘conservative’ PDF concept in the global fits of PDFs and SMEFT Wilson coefficients, and study the impact of using simultaneously-determined ‘SMEFT’ PDFs to make precise theoretical predictions in searches for New Physics. In Section 4 we identify several best-practice recommendations to the HEP community. Finally in Section 5 we summarise our findings and plans for future work.

## 2 A toy model for global PDF and SMEFT fits

In this section, we introduce a toy model for global PDF and SMEFT fits which motivates the phenomenological study we perform in the sequel. Throughout this section we work with two data points, one which is used for PDF fitting (the PDF itself is considered to be a single real variable  $f$ ), and one which is used for SMEFT fitting (we work with a single SMEFT Wilson coefficient  $c$ ). This crude model is sufficient to demonstrate some of the key behaviour which is investigated in realistic cases later in this work and has the advantage of being analytically tractable to some extent.

In Sect. 2.1, we present the toy model. Subsequently, in Sect. 2.2, we derive analytic expressions for the posterior distributions of PDFs and Wilson coefficients in both separate and simultaneous fits. Finally, in Sect. 2.3, we present and discuss the results of both types of fit in this toy model with a numerical example.

### 2.1 Presentation of the model

Assuming collinear factorization, we can – very schematically – model a theoretical prediction for a collider observable  $\mathcal{O}$  that is sensitive to a given SMEFT Wilson coefficient  $c$  and to a single parton channel as

$$t(f, c) = s_{\text{SM}} (f_{\text{ref}} + f) (1 + c s_{\text{lin}}), \quad (2.1)$$

where  $s_{\text{SM}}$  represents the SM partonic cross section,  $(f_{\text{ref}} + f)$  represents the given parton luminosity channel that the observable is sensitive to and  $s_{\text{lin}}$  is the linear SMEFT  $K$ -factor accounting for the interference between the SM amplitude and the SMEFT amplitude. The parton luminosity entering Eq. (2.1) is decomposed into two contributions. The term  $f_{\text{ref}}$  represents a fixed reference luminosity taken from an input PDF set, while  $f$  parametrises a shift of this luminosity induced by including the observable  $\mathcal{O}$  in a PDF fit. Expanding Eq. (2.1) we obtain

$$\begin{aligned} t(f, c) &= s_{\text{SM}} f_{\text{ref}} + s_{\text{SM}} f + s_{\text{SM}} f_{\text{ref}} s_{\text{lin}} c + s_{\text{SM}} s_{\text{lin}} f c \\ &= \tilde{t}_0 + \tilde{t}_f f + \tilde{t}_c c + \tilde{t}_i f c. \end{aligned} \quad (2.2)$$

The interpretation of the above expression is quite straightforward: the first term  $\tilde{t}_0 = s_{\text{SM}} f_{\text{ref}}$  is the SM prediction for the observable  $\mathcal{O}$  obtained with a fixed input PDF set; the second term  $\tilde{t}_f f$ , with  $\tilde{t}_f = s_{\text{SM}}$ , is the part of the SM predictions that varies once the observable  $\mathcal{O}$  – sensitive on a particular luminosity channel – is included in a PDF fit, and the coefficient  $\tilde{t}_f$  can be associated to the sensitivity of the observable to the PDFs; the third term  $\tilde{t}_c$  with  $\tilde{t}_c = s_{\text{SM}} f_{\text{ref}} s_{\text{lin}}$  is the linear SMEFT contribution suppressed by two powers of the heavy new physics scale  $\Lambda^2$ , which varies with  $c$  once the observable  $\mathcal{O}$  is included in a SMEFT fit, and the coefficient  $\tilde{t}_c$  can be associated to the sensitivity of the observable to SMEFT corrections; the last term  $\tilde{t}_i f c$ , with  $\tilde{t}_i = s_{\text{SM}} s_{\text{lin}}$ , captures the interplay between PDF and SMEFT effects. It accounts for the fact that the SMEFT contribution itself is modulated by shifts in the parton luminosity, and therefore encodes the strength of the correlation between PDF determination and SMEFT inference. This term is typically neglected in pure PDF fits (in which  $c = 0$ ) and in pure SMEFT fits (where PDFs are held fixed to some  $f_{\text{ref}}$ , hence  $f = 0$ ).

To keep the model analytically tractable we exploit the fact that  $\tilde{t}_i$  is typically much smaller than  $\tilde{t}_f$  and  $\tilde{t}_c$ , as  $\tilde{t}_i$  is doubly suppressed, both by the  $\Lambda^2$  in the denominator of  $s_{\text{lin}}$  and by the size of the change in the PDFs associated with  $f$ , which is much smaller than the PDFs themselves<sup>1</sup>. We can therefore expand Eq. (2.2) around  $(f_0, c_0)$ , which are the maximum likelihood estimators (MLE) of the theory  $t(f, c)$  when  $\tilde{t}_i$  is set to 0 – which we will henceforth refer to as *linear* theory. Consider the first-order Taylor expansion of the full theory Eq. (2.2),

$$t(f, c) \simeq t(f_0, c_0) + \left. \frac{\partial t}{\partial f} \right|_{(f_0, c_0)} (f - f_0) + \left. \frac{\partial t}{\partial c} \right|_{(f_0, c_0)} (c - c_0). \quad (2.3)$$

Given that  $\partial t / \partial f = \tilde{t}_f + \tilde{t}_i c$  and  $\partial t / \partial c = \tilde{t}_c + \tilde{t}_i f$  we can define the *effective linear sensitivities* as the local slopes of the full model around  $(f_0, c_0)$ ,

$$\begin{aligned} t_f &\equiv \tilde{t}_f + \tilde{t}_i c_0, \\ t_c &\equiv \tilde{t}_c + \tilde{t}_i f_0, \end{aligned} \quad (2.4)$$

---

<sup>1</sup>The inclusion of a new dataset in a PDF fit typically shifts the PDFs by no more than 10% compared to the value of the PDFs before the inclusion of such dataset.

and the linearised expression becomes

$$t(f, c) \simeq t_0 + t_f f + t_c c, \quad (2.5)$$

where the constant term  $\tilde{t}_0$  of Eq. (2.2) is shifted to  $t_0$  by a term that is suppressed by  $\tilde{t}_i$ . The expansion of Eq. (2.5) shows that, in the small- $\tilde{t}_i$  limit, the non-linear PDF–EFT interplay term proportional to  $\tilde{t}_i$  in the full theory (2.2) can be interpreted as a redefinition of the linear sensitivities around the MLE of a theory in which the interaction term proportional to  $\tilde{t}_i$  is completely neglected. This parametrisation has the advantage that the toy model becomes analytically tractable, giving us some simple parametric understanding of what happens in a PDF-SMEFT fit<sup>2</sup>.

We now consider two observables and their respective measurements, that are collected into a vector of two data points  $\mathbf{d} = (d_1, d_2)^T$ , which we assume are distributed according to a multivariate normal distribution centred around our theoretical model

$$\mathbf{d} = \begin{pmatrix} d_1 \\ d_2 \end{pmatrix} \sim \mathcal{N}(\mathbf{t}(f, c), \Sigma_{\text{exp}}), \quad (2.6)$$

where  $\mathbf{t} : \mathbb{R}^2 \rightarrow \mathbb{R}^2$  is the linear theory prediction given by Eq. (2.5), where now the effective  $\mathbf{t}_f$  and  $\mathbf{t}_c$  sensitivities are a 2-dimensional vector, hence the boldface, each component being defined as in Eq. (2.4).

The experimental covariance matrix  $\Sigma_{\text{exp}}$  is a  $2 \times 2$  matrix, which for simplicity does not contain correlations between the data points:

$$\Sigma_{\text{exp}} = \begin{pmatrix} \sigma_1^2 & 0 \\ 0 & \sigma_2^2 \end{pmatrix}. \quad (2.7)$$

The dataset  $\mathbf{d} = (d_1, d_2)^T$  is intended to be a gross simplification of a global particle physics dataset. In particular, this dataset can be split into two sets:

- The first data point  $d_1$  can be regarded as the ‘*PDF fitting dataset*’; that is, it contains the data which is usually used to infer SM PDFs. It may be interpreted as a low energy measurement in  $Q^2$ , where the effects of heavy new physics are very small or negligible.
- The second data point  $d_2$  can be regarded as the ‘*SMEFT fitting dataset*’; that is, it contains the data which is usually used by SMEFT fitting collaborations to infer the SMEFT Wilson coefficients. It may be interpreted as a high energy measurement in  $Q^2$ .

There are two main modes of fitting, given this categorisation of the data.

- (1) SEPARATE FIT. The PDF parameter and the Wilson coefficient are determined in two distinct steps, without ever maximising a joint likelihood in  $(f, c)$ , namely  $f$  is

---

<sup>2</sup>In a realistic fits, however, we account for the interaction term, as implemented in the SIMUnet methodology.

inferred under the assumption that the Wilson coefficient  $c$  vanishes, and the Wilson coefficient  $c$  is determined from the relevant high energy data, either by fixing the PDF parameter  $f$  to the obtained best-fit value or by marginalising over its distribution (the latter accounts for PDF uncertainty, as is often done in SMEFT fits). Depending on which data are used in the PDF determination, this strategy can take two forms.

If the PDF is extracted exclusively from data whose theory predictions depend only very weakly on the Wilson coefficient (e.g. low energy data), the procedure is referred to as a *conservative* fit. For example, the SMEFT collaboration [23–27] uses PDF sets that exclude top data when determining top-sector SMEFT Wilson coefficients [28], thereby avoiding overlap between the dataset entering the PDF fit and the dataset entering the SMEFT fit.

On the other hand, if SMEFT-sensitive data is included in the PDF determination while setting  $c = 0$ , then potential BSM effects can be absorbed into the PDF parametrisation. In this case, the resulting fit is referred to as *BSM-biased*.

- (2) **SIMULTANEOUS FIT.** The PDFs and Wilson coefficient are jointly determined using both the first and second data points and including both linear terms in the theory prediction  $\mathbf{t}$ . This represents the type of fit that has been explored in several works, including [6, 7, 10, 29], and we dub it as *simultaneous* fit.

In the next section we explore both these options and compare and contrast the results that we obtain in the simple model that we have defined here.

## 2.2 Analytic derivations

In this subsection we discuss the analytic structure underlying the separate and simultaneous fitting strategies introduced above. The goal is to explore the origin of the PDF-SMEFT interplay in a simple Gaussian model that is analytically tractable. Throughout, we work in the linearised theory defined in Eq. (2.5) and consider the measurements described in the previous subsection, in the specific case in which  $d_1$  is a low energy measurement that is weakly sensitive to the SMEFT coefficient  $c$ , while  $d_2$  is a high energy measurement that is highly sensitive to  $c$ <sup>3</sup>. Both measurements are sensitive to the PDFs in the same parton channel and in the same large  $x$ - region of the PDFs. In what follows, we discuss the separate conservative fit, separate BSM-biased fit, and simultaneous fit.

**Separate conservative fit.** In the conservative strategy, the PDF parameter  $f$  is determined solely from the low-energy observable  $d_1$ , assuming  $c = 0$ . The corresponding likelihood is

$$\mathcal{L}_1(d_1 | f) \propto \exp \left[ -\frac{1}{2} \frac{(d_1 - t_{0,1} - t_{f,1}f)^2}{\sigma_1^2} \right],$$

where  $t_{0,1}$  is the first component of the  $\mathbf{t}_0$  vector, and so on. Maximisation yields the best-fit value  $\hat{f}$  and its variance  $\sigma_f^2$  such that

---

<sup>3</sup>At sufficiently low energy, EFT effects are typically negligible. Here we retain a small but non-zero sensitivity in  $d_1$  to explore the differences between the separate and simultaneous fitting methodologies.

$$\hat{f}_{\text{cons}} = \frac{d_1 - t_{0,1}}{t_{f,1}}, \quad \sigma_{f_{\text{cons}}}^2 = \frac{\sigma_1^2}{(t_{f,1})^2}. \quad (2.8)$$

Using this PDF determination, the SMEFT coefficient  $c$  is extracted from the high energy observable  $d_2$ , yielding a best-fit value of

$$\hat{c}_{\text{cons}} = \frac{d_2 - t_{0,2} - t_{f,2}\hat{f}_{\text{cons}}}{t_{c,2}}.$$

If the PDF uncertainty is not propagated, the resulting variance is

$$\sigma_{c_{\text{cons, no PDF}}}^2 = \frac{\sigma_2^2}{(t_{c,2})^2}. \quad (2.9)$$

A more conservative treatment marginalises over the PDF uncertainty obtained from  $d_1$ , which simply increases the variance entering the  $\chi^2$ . The resulting uncertainty on the SMEFT coefficient becomes

$$\sigma_{c_{\text{cons, with PDF}}}^2 = \frac{\sigma_2^2 + t_{f,2}^2 \sigma_{f_{\text{cons}}}^2}{t_{c,2}^2} = \sigma_{c_{\text{cons, no PDF}}}^2 \left( 1 + t_{f,2}^2 \frac{\sigma_{f_{\text{cons}}}^2}{\sigma_2^2} \right), \quad (2.10)$$

where we have used Eq. (2.9) and factorised a degradation coefficient that is related to the PDF uncertainty. Thus, in the conservative fit, failing to propagate PDF uncertainty can lead to an overestimate of the precision in  $c$ . The impact is controlled by the combination  $t_{f,2}^2 \sigma_{f_{\text{cons}}}^2$ . If  $d_2$  is only weakly sensitive to the PDFs or if the PDF is very precisely determined, the effect is negligible. Conversely, when the high energy observable has strong PDF sensitivity and the PDF uncertainty is sizeable, the constraint on  $c$  is correspondingly degraded.

**Separate BSM-biased fit.** In the BSM-biased strategy, the PDF parameter  $f$  is extracted from both  $d_1$  and  $d_2$  under the SM assumption  $c = 0$ . In this case, the PDF best-fit value is given by

$$\hat{f}_{\text{bias}} = \frac{t_{f,1}(d_1 - t_{0,1})/\sigma_1^2 + t_{f,2}(d_2 - t_{0,2})/\sigma_2^2}{D_f}, \quad D_f \equiv \frac{t_{f,1}^2}{\sigma_1^2} + \frac{t_{f,2}^2}{\sigma_2^2}, \quad (2.11)$$

with a corresponding variance

$$\sigma_{f_{\text{bias}}}^2 = \frac{1}{D_f}.$$

Notably, since  $D_f > (t_{f,1}/\sigma_1)^2$ , we find that

$$\sigma_{f_{\text{bias}}}^2 < \sigma_{f_{\text{cons}}}^2, \quad (2.12)$$

where we have used the variance of Eq. (2.8). In this way, the PDF uncertainty is reduced with respect to the conservative case. Notice that if the true underlying SMEFT coefficient satisfies  $c_{\text{true}} \neq 0$ , this procedure induces a systematic bias in the extracted PDF,

$$\text{bias}(\hat{f}_{\text{bias}}) \equiv \mathbb{E}[\hat{f}_{\text{bias}}] - f_{\text{true}} = c_{\text{true}} \frac{t_{f,1}t_{c,1}/\sigma_1^2 + t_{f,2}t_{c,2}/\sigma_2^2}{t_{f,1}^2/\sigma_1^2 + t_{f,2}^2/\sigma_2^2}, \quad (2.13)$$

which is, intuitively, proportional to the true underlying SMEFT coefficient  $c_{\text{true}}$ . This bias also increases with the SMEFT sensitivity of the datapoints so, even if the low-energy observable is only weakly sensitive (or not sensitive at all) to the SMEFT coefficient, the high energy measurement (where SMEFT effects are usually enhanced) induces a non-vanishing bias.

Fitting  $c$  solely from  $d_2$  using the biased PDF result leads to

$$\hat{c}_{\text{bias}} = \frac{d_2 - t_{0,2} - t_{f,2} \hat{f}_{\text{bias}}}{t_{c,2}}, \quad (2.14)$$

with a propagated bias from the PDF sector which translates into a SMEFT bias of

$$\text{bias}(\hat{c}_{\text{bias}}) \equiv \mathbb{E}[\hat{c}_{\text{bias}}] - c_{\text{true}} = -\frac{t_{f,2}}{t_{c,2}} \text{bias}(f), \quad (2.15)$$

where we see that the bias in  $c$  is therefore directly proportional in size to the bias in  $f$ , with a coefficient controlled by the relative sensitivities  $t_{f,2}$  and  $t_{c,2}$  at high energy. Intuitively, an overestimate (underestimate) of the PDF contribution at high energy is compensated by an underestimate (overestimate) of the EFT contribution. Notice that by propagating PDF uncertainty the SMEFT uncertainty becomes

$$\sigma_{c_{\text{bias}}, \text{ with PDF}}^2 = \frac{\sigma_2^2 + t_{f,2}^2 \sigma_{f,\text{bias}}^2}{t_{c,2}^2}, \quad (2.16)$$

where comparison with Eq. (2.9) yields

$$\sigma_{c_{\text{bias}}}^2 < \sigma_{c_{\text{cons}}}^2, \quad (2.17)$$

where we see that the BSM-biased fit therefore produces both smaller quoted uncertainties and a systematic bias whenever  $c_{\text{true}} \neq 0$ .

**Simultaneous fit.** In the simultaneous strategy, the PDF parameter  $f$  and the EFT coefficient  $c$  are determined jointly from the two measurements  $(d_1, d_2)$ . In this case, it is convenient to write the problem in matrix form. Defining the data vector with constant pieces subtracted,

$$\mathbf{d} \equiv \begin{pmatrix} d_1 - t_{0,1} \\ d_2 - t_{0,2} \end{pmatrix},$$

the parameter vector

$$\boldsymbol{\theta} \equiv \begin{pmatrix} f \\ c \end{pmatrix},$$

and the  $2 \times 2$  feature (design) matrix

$$X \equiv \begin{pmatrix} t_{f,1} & t_{c,1} \\ t_{f,2} & t_{c,2} \end{pmatrix},$$

the Gaussian log-likelihood is equivalent to the weighted least-squares objective

$$\chi^2(\boldsymbol{\theta}) = (\mathbf{d} - X\boldsymbol{\theta})^T V^{-1} (\mathbf{d} - X\boldsymbol{\theta}), \quad (2.18)$$

with  $V = \text{diag}(\sigma_1^2, \sigma_2^2)$ . The maximum-likelihood estimator admits (assuming basic invertibility conditions) the closed-form solution

$$\hat{\boldsymbol{\theta}} = (X^T V^{-1} X)^{-1} X^T V^{-1} \mathbf{d}. \quad (2.19)$$

Writing  $X^T V^{-1} X = \begin{pmatrix} A & B \\ B & C \end{pmatrix}$  with

$$A \equiv \frac{t_{f,1}^2}{\sigma_1^2} + \frac{t_{f,2}^2}{\sigma_2^2}, \quad (2.20)$$

$$B \equiv \frac{t_{f,1} t_{c,1}}{\sigma_1^2} + \frac{t_{f,2} t_{c,2}}{\sigma_2^2}, \quad (2.21)$$

$$C \equiv \frac{t_{c,1}^2}{\sigma_1^2} + \frac{t_{c,2}^2}{\sigma_2^2}, \quad (2.22)$$

and  $\Delta \equiv AC - B^2 > 0$ , the individual estimators are

$$\hat{f}_{\text{sim}} = \frac{C u - B v}{\Delta}, \quad \hat{c}_{\text{sim}} = \frac{A v - B u}{\Delta}, \quad (2.23)$$

where  $u$  and  $v$  are the corresponding weighted data combinations given by

$$u \equiv \frac{t_{f,1}(d_1 - t_{0,1})}{\sigma_1^2} + \frac{t_{f,2}(d_2 - t_{0,2})}{\sigma_2^2},$$

$$v \equiv \frac{t_{c,1}(d_1 - t_{0,1})}{\sigma_1^2} + \frac{t_{c,2}(d_2 - t_{0,2})}{\sigma_2^2}.$$

Note that the covariance matrix of the estimator is

$$\text{Cov}_{\text{sim}}(f, c) = (X^T V^{-1} X)^{-1} = \frac{1}{\Delta} \begin{pmatrix} C & -B \\ -B & A \end{pmatrix}, \quad (2.24)$$

implying correlated uncertainties for  $f$  and  $c$ , *even* if  $d_1$  and  $d_2$  are uncorrelated (or if their correlations are neglected, in a real dataset). Also (although trivially) by construction the MLE values in the simultaneous fit are unbiased. The data have been generated according to the same underlying model used in the simultaneous fit, as in a closure test setting in the PDF nomenclature.

### 2.3 Results

In this subsection we illustrate the analytic results derived above by applying the three fitting strategies to a concrete toy example. The purpose is to visualise the impact of PDF-EFT interplay on both central values and uncertainties, and to contrast conservative, BSM-biased, and simultaneous fits in a controlled setting.

We assume that the pseudodata are generated from the linearised model, Eq. 2.5, with true underlying parameters

$$f_{\text{true}} = 10.0, \quad c_{\text{true}} = 0.1. \quad (2.25)$$

The theory coefficients are fixed to

$$\mathbf{t}_0 = (0.1, 0.1), \quad \mathbf{t}_f = (0.1, 0.1), \quad \mathbf{t}_c = (0.1, 1.0), \quad (2.26)$$

so that the first observable  $d_1$  is dominantly sensitive to the PDF parameter  $f$ , while the second observable  $d_2$  exhibits enhanced sensitivity to the EFT coefficient  $c$ . Experimental uncertainties are taken to be uncorrelated and proportional to the true central values, with a relative size of 1%. For clarity, the pseudodata are set equal to their expectation values, so that all differences between the fits arise solely from modelling assumptions rather than statistical fluctuations.

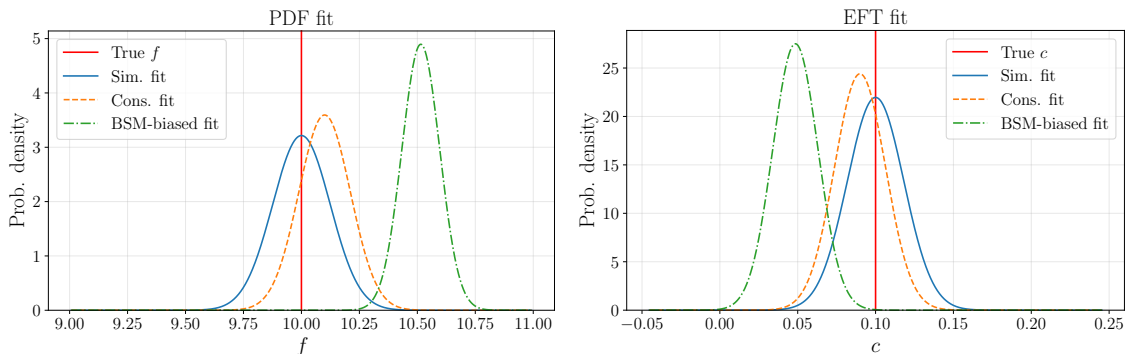


**Figure 2.1.** One-dimensional posterior distributions for the PDF parameter  $f$  (left) and the EFT coefficient  $c$  (right) obtained in the toy model. The red vertical lines indicate the true values ( $f_{\text{true}}, c_{\text{true}}$ ). The conservative fit is unbiased but exhibits inflated uncertainties, the BSM-biased fit yields artificially precise yet shifted posteriors, and the simultaneous fit correctly recovers both parameters in this closure-test configuration.

Figure 2.1 compares the one-dimensional posterior distributions for the PDF parameter  $f$  (left) and the EFT coefficient  $c$  (right) obtained using the three fitting strategies discussed in Sec. 2.2. We begin with the *simultaneous fit*, which serves as the reference or “golden standard”. In this case,  $f$  and  $c$  are inferred jointly, fully exploiting the information content of both observables (and their correlations in a more realistic dataset, as we will see later in the text). As expected from the analytic results, the simultaneous fit yields unbiased estimates for both parameters.

The *conservative fit* provides the next best alternative. Here, the PDF parameter  $f$  is determined using only the low energy observable  $d_1$ , and the resulting PDF uncertainty is consistently propagated into the determination of  $c$  from the high energy observable  $d_2$ . This strategy sacrifices sensitivity relative to the simultaneous fit, leading to broader posteriors for both  $f$  and  $c$ , but it remains robust: the extracted values are close to the true parameters ( $f_{\text{true}}, c_{\text{true}}$ ). The loss of precision can be directly traced to the deliberate exclusion of  $d_2$  from the PDF determination.

Finally, the *BSM-biased fit* illustrates the failure mode identified analytically in Sec. 2.2. In this case, both  $d_1$  and  $d_2$  are used to constrain the PDF under the incorrect assumption  $c = 0$ . Because the high energy observable  $d_2$  has strong sensitivity to the EFT coefficient, its constraining power artificially reduces the PDF uncertainty, producing a posterior for

$f$  that is both shifted away from  $f_{\text{true}}$  and spuriously narrow. This overconstrained and biased PDF determination is then propagated into the EFT fit, yielding a posterior for  $c$  that is likewise displaced from  $c_{\text{true}}$  (in the opposite direction) and exhibits a smaller uncertainty than in the conservative case. The result is an incorrect determination: the apparent gain in precision is entirely spurious and arises from absorbing genuine EFT effects into the PDF fit.

These toy model results provide a controlled illustration of how PDF-EFT interplay, bias, and uncertainty propagation arise in separate and simultaneous fits; in the next section, we extend this analysis to realistic new physics scenarios in the context of the HL-LHC.

### 3 Disentangling new physics signals and PDFs at the HL-LHC

In this section, we start by presenting the methodological setup adopted in this analysis, including the simultaneous closure-test framework and the full set of data and HL-LHC projections considered (Sect. 3.1). We then examine two benchmark BSM scenarios separately: one primarily affecting the quark sector at large  $x$  via Drell-Yan high-mass measurements (Sect. 3.2) and one impacting the gluon sector at large  $x$  via measurements of top pair production at large invariant mass (Sect. 3.3). For each scenario, we demonstrate how the corresponding BSM signal can be partially absorbed into the PDFs, in the quark and gluon sectors respectively, thereby introducing a source of bias. We then perform a comparative assessment of the extent to which the use of conservative PDFs, or alternatively a simultaneous fit of PDFs and SMEFT coefficients mitigates the resulting BSM-induced bias in the extracted constraints.

#### 3.1 Analysis settings

Our analysis is based on the *simultaneous closure test* framework [6, 14], which extends the PDF closure-test methodology introduced in Refs. [30–32]. The framework consists of a three-step procedure:

- (i) In the first step, a PDF set  $\mathbf{f}_{\text{true}}$  is selected and identified as the *true* underlying PDFs, together with a BSM model defining the *true* law of nature. When applicable, BSM effects are parametrised in terms of a set of SMEFT Wilson coefficients  $\mathbf{c}_{\text{true}}$ ; synthetic data, referred to as Level-0 ( $L_0$ ) data, are then generated according to

$$\mathbf{D}^0 = T[\mathbf{f}_{\text{true}}, \mathbf{c}_{\text{true}}] = \hat{\sigma}_{\text{NNLO}}^{\text{SM}} \otimes \mathcal{L}_{\text{true}} \left[ 1 + \sum_i c_i^{\text{true}} R_i \right],$$

where  $\hat{\sigma}_{\text{NNLO}}^{\text{SM}}$  denotes the vector of partonic cross sections computed at NNLO in perturbative QCD within the SM, and  $\mathcal{L}_{\text{true}}$  are the parton luminosities constructed from the *true* PDFs. The term in brackets accounts for BSM contributions through the corresponding linear SMEFT  $K$ -factors  $R_i$ , computed with the *true* PDFs; the synthetic observables  $\mathbf{D}^0$  are assigned uncertainties and correlations according to the experimental covariance matrices of the measurements or projections included in the fit.

- (ii) In the second step, a simultaneous fit to the synthetic data is performed, in which both the PDFs and the Wilson coefficients parametrising the BSM model are treated as free parameters and determined concurrently.
- (iii) In the third step, the fitted PDFs and Wilson coefficients are compared to the corresponding *true* PDF and *true* SMEFT coefficient values used as input in the generation of the synthetic data. The simultaneous closure test is deemed successful if the fitted results are statistically compatible with the underlying law of nature within the quoted uncertainties.

Simultaneous closure tests probe the ability of a joint PDF–SMEFT fitting procedure to disentangle distortions induced by potential BSM effects from genuine PDF features. This framework is particularly well suited to isolating the interplay between PDFs and BSM contributions. By construction, the synthetic data are internally consistent and their theoretical description is exact. As a result, additional effects arising from experimental tensions between datasets [32] or from missing higher-order corrections in the SM predictions [33, 34] are absent.

From an experimental perspective, we generate a synthetic dataset comprising a total of 4363 data points, covering a broad range of processes. The  $L_0$  data constructed according to Eq. (3.1) are drawn from two sources:

1. Observables currently included in the NNPDF4.0 analysis [35], excluding all jet observables so that we can isolate the top data and use them as the main source of constraints for the large- $x$  gluon. Moreover we supplement the NNPDF4.0 dataset by the Drell–Yan and top-quark measurements incorporated in Refs. [4, 6] and [10], respectively. After applying kinematic cuts, this dataset comprises  $n_{\text{data}}^{\text{current}} = 4271$  data points.
2. Projections for the HL-LHC in high-mass Drell–Yan, forward Drell–Yan, and high-mass top-pair production, yielding a total of  $n_{\text{data}}^{\text{HL}} = 92$  data points. The uncertainties associated with the first category are taken directly from the corresponding experimental publications and therefore reflect realistic experimental conditions. In contrast, the uncertainties assigned to the HL-LHC projections are constructed following dedicated projection scenarios, which are described in detail later in this section.

The kinematic coverage of the data points used in this study is shown in Fig. 3.1. The points are shown in  $(x, Q^2)$  space with the HL-LHC projections highlighted with a border. The high-mass Drell-Yan, forward on-shell Drell-Yan and top quark pair production HL-LHC projections that we generate are summarised in Tab. 3.1, Tab. 3.2 and Tab. 3.3, and illustrated below.

**HL-LHC high-mass Drell-Yan (HMDY) projections** The invariant mass distribution projections are generated at  $\sqrt{s} = 14$  TeV, assuming an integrated luminosity of  $\mathcal{L} = 6 \text{ ab}^{-1}$  (  $3 \text{ ab}^{-1}$  collected by ATLAS and  $3 \text{ ab}^{-1}$  by CMS). Both in the case of NC and CC Drell-Yan cross sections, the pseudodata were generated using the `MadGraph5_aMCatNLO`

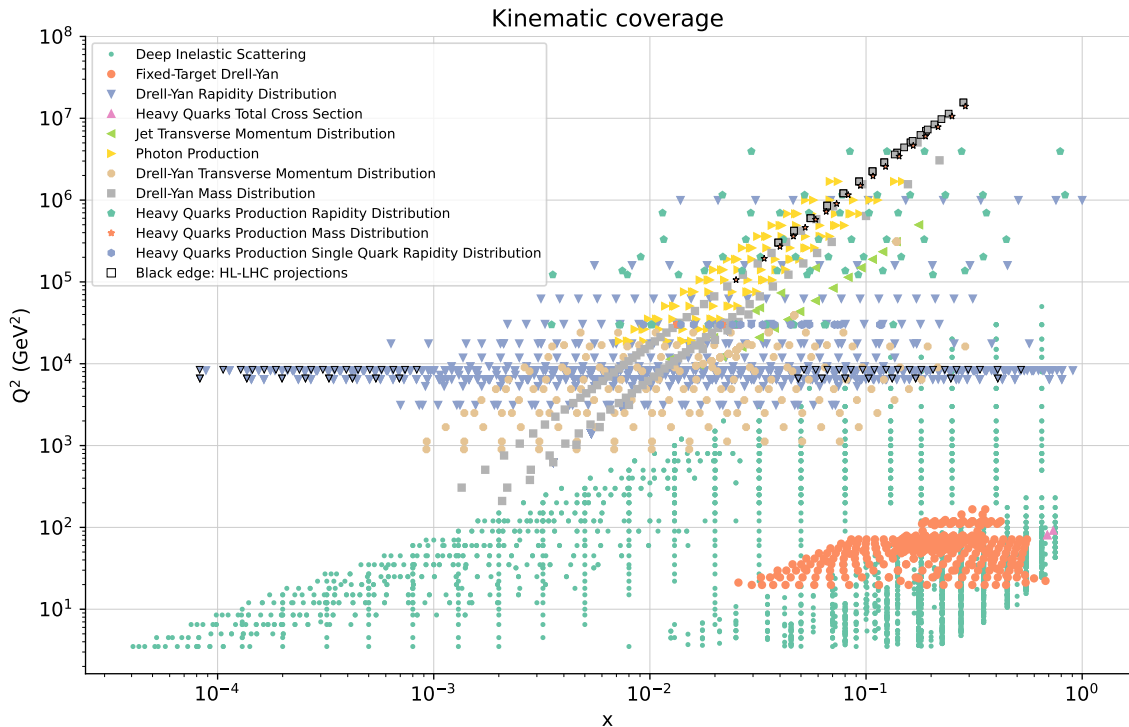


**Figure 3.1.** Kinematic coverage of the data points included in the PDF fit. The points highlighted with a black edge are our HL-LHC projections, while the other data points correspond to existing measurements. The values of  $x$  have been computed using a leading order approximation.

NLO Monte Carlo event generator [36] with additional  $K$ -factors to include the NNLO QCD and mass-dependent NLO EW corrections. The pseudodata consist of four datasets (associated with NC/CC distributions with muons/electrons in the final state), each comprising respectively 12 (NC) and 16 (CC) bins in the  $m_{ll}$  invariant mass distribution or transverse mass  $m_T$  distributions with both  $m_{ll}$  and  $m_T$  greater than 500 GeV, with the highest energy bins reaching  $m_{ll} = 4$  TeV ( $m_T = 3.5$  TeV) for NC (CC) data. The rationale behind the choice of number of bins and the width of each bin was outlined in Ref. [37], and stemmed from the requirement that the expected number of events per bin was big enough to ensure the applicability of Gaussian statistics. The choice of binning for the  $m_{ll}$  ( $m_T$ ) distribution at the HL-LHC is displayed in Fig. 5.1 of Ref. [37].

Process	$N_{\text{dat}}$	$m$ [GeV]	Ref.
High-mass Drell-Yan (NC)	12	$m_{\ell\ell} \in [500, 4600]$	[37]
High-mass Drell-Yan (CC)	16	$m_T \in [500, 3500]$	[37]

**Table 3.1.** High-mass Drell-Yan projections at the HL-LHC already presented in [37] and already included in [11].

**HL-LHC forward Drell-Yan projections** HL-LHC projections for LHCb are generated assuming an integrated luminosity of  $0.3 \text{ ab}^{-1}$  as a benchmark, and focus on for-

ward  $W$  and  $Z$  production. The predictions for each process were generated using the `MadGraph5_aMCatNLO` NLO Monte Carlo event generator [36] interfaced with `Pipeline` [38] with additional  $K$ -factors to include the NNLO QCD correction produced using `NNLOJET` [39]. The  $Z$  boson is produced on-shell ( $60 \text{ GeV} < m_{ll} < 120 \text{ GeV}$ ). In both processes we impose requirements on the transverse momentum ( $p_T^l > 20 \text{ GeV}$ ) and on the rapidity to study the forward region ( $2 < |y| < 4.5$ ) following the selections used in Ref. [40]. In Ref. [11], we showed that these data primarily constrain the  $u$  and  $d$  quark PDFs, while providing only limited sensitivity to the light antiquark distributions. This can be understood from the kinematics of forward lepton production at LHCb: for the final-state leptons to populate the forward region, one of the initial-state partons must carry a significantly larger longitudinal momentum fraction than the other. Since quarks are far more likely than antiquarks to carry a large fraction of the proton momentum, the resulting constraints predominantly affect the quark sector.

Process	$N_{\text{dat}}$	$y$	Ref.
Forward Drell–Yan (NC)	18	$y_Z \in [2.0, 4.5]$	[40]
Forward Drell–Yan (CC)	8	$y_\mu \in [2.0, 4.5]$	[40]

**Table 3.2.** Forward on-shell Drell–Yan HL-LHC projections generated for this study and inspired by the existing LHCb measurements of Ref. [40].

**HL-LHC top quark pair production** The LHC operates as a top-quark factory, producing very large samples of  $t\bar{t}$  events as well as sizeable datasets for rarer top-quark processes. The prospects for measurements at the HL-LHC, corresponding to an integrated luminosity of  $3 \text{ ab}^{-1}$ , are taken from Ref. [41], which in turn were obtained through an extrapolation of current Run II results.

In the projection scenario considered in Ref. [41], statistical uncertainties and a subset of experimental systematic uncertainties are assumed to scale with the inverse square root of the integrated luminosity, while the remaining experimental systematics are reduced by an overall factor of five. In this work, we focus on differential measurements of the  $t\bar{t}$  production cross section as a function of the invariant mass of the  $t\bar{t}$  system. Such measurements at large invariant mass already play a central role in constraining four-fermion operators. To fully exploit the HL-LHC potential, the kinematic reach of the projections in the  $t\bar{t}$  invariant mass is extended from the current upper limit of approximately 1.5 TeV to 3 TeV. Theoretical predictions for these observables are computed at NNLO in QCD for the SM, using `fastNLO` grids [42] supplemented by NNLO/NLO  $K$ -factors computed with the `HighTea` tool [43], while the SMEFT contributions are included at leading order through the corresponding  $K$ -factors.

Process	$N_{\text{dat}}$	$m_{t\bar{t}}$ [GeV]	Ref.
High-mass $t\bar{t}$ production	18	$m_{t\bar{t}} \in [250, 3000]$	[41]

**Table 3.3.** Top-pair projections at the HL-LHC, from Ref. [41].

The impact of the HL-LHC projections on the PDFs is assessed in Fig. 3.2 by comparing a fit on  $L_0$  data one including the HL-LHC projections (orange band) and one excluding them (green band). A substantial reduction in the uncertainties of the quark–antiquark luminosity is observed at invariant masses above 1 TeV, indicating that the HL-LHC Drell–Yan projections play a dominant role in constraining the quark and antiquark PDFs in the large- $x$  region. By contrast, the effect of the HL-LHC top-quark projections on the gluon–

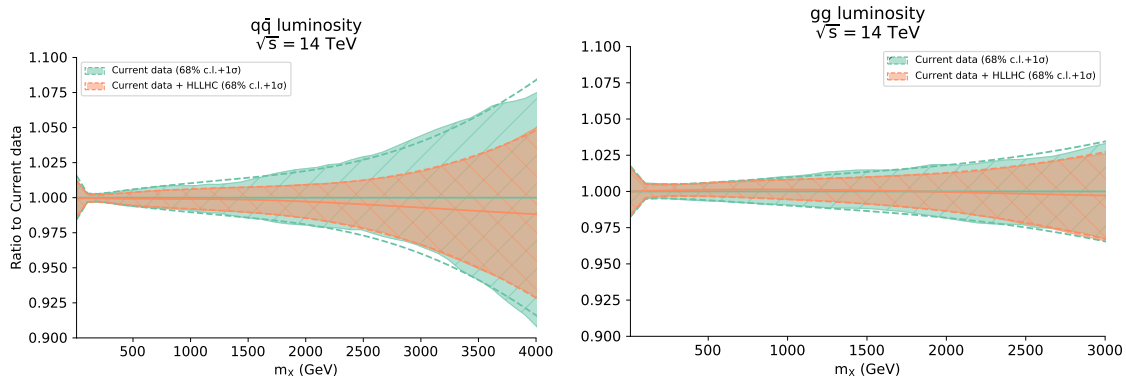


**Figure 3.2.** Impact of the HL-LHC projections on the uncertainties of the quark-antiquark (left) and gluon-gluon (right) PDF luminosities.

gluon luminosity is significant, but less stringent in comparison to the high-mass Drell-Yan distributions. This suggests that the current extensive top-quark data already included in the fit, which was implemented in [10] remain competitive with the HL-LHC projections in constraining the gluon PDF at large  $x$ .

### 3.2 BSM and PDF interplay in the Drell-Yan sector

In this section we consider two BSM scenarios, that can be parametrised in the SMEFT, impacting the Drell-Yan sector: the oblique parameters  $\hat{W}$  (corresponding to a heavy universally coupled  $W'$  field) and  $\hat{Y}$  (corresponding to a heavy universally coupled  $Z'$  field), playing a role similar to the  $c$  coefficient introduced in Sect. 2.1. More details on the models are given in App. A.1 and App. A.2 respectively. These models have already been explored in the context of PDF fitting in Refs. [4, 6, 11, 12], where it was shown that – within a global PDF fit – synthetic data generated with a non-zero  $\hat{Y}$  injected would be flagged as incompatible with the bulk of the data included in the fit, whereas the injection of a non-zero  $\hat{W}$  in the high-energy tails of the HL-LHC measurements could be completely absorbed by the PDFs if those were fitted by assuming the SM, hence producing *BSM-biased* PDFs. Throughout this section, we analyse the results in the context of a closure test in which the *true* underlying law that we use to generate the synthetic data is given by the NNPDF4.0 NNLO PDF set [44] – which we assume to be the *true* PDFs – and the *true* theory of nature is given by the SM augmented by new heavy universally-coupled boson(s) that can be parametrised at the LHC energies in the SMEFT by a combination of non-zero  $\hat{Y}$  and  $\hat{W}$  Wilson coefficients that we will specify in the text.

The current Run I and Run II high-mass Drell–Yan measurements that we include in our analysis, comprising neutral-current Drell–Yan measurements performed by ATLAS at  $\sqrt{s} = 7$  and 8 TeV [45, 46] and by CMS at  $\sqrt{s} = 7, 8$  and 13 TeV [47–49], are sensitive to the BSM scenario considered here [50]. The HL-LHC high-mass projections enhance by a large factor the current sensitivity. In Fig. 3.3 we show the deviation from the SM predictions that the HL-LHC projections would display if a new heavy universally-coupled  $W'$  boson with mass  $M_{W'} = 13.8$  TeV was present in nature (corresponding to a SMEFT Wilson coefficient  $\hat{W} = 8 \times 10^{-5}$ ). We observe that the distortion in the tails is larger than (comparable to) the uncertainty of the SM theoretical predictions for masses above 1 TeV in the case of charged (neutral) current. In the case of charged currents the SM uncertainty – for invariant mass around 500 GeV – is dominated by the experimental uncertainties while above 2 TeV the PDF uncertainty is dominant with respect to the experimental one. In the case of neutral current PDF uncertainties are smaller than the experimental ones across the whole  $m_{\ell\ell}$  spectrum, and are dominated by systematic uncertainties. On the

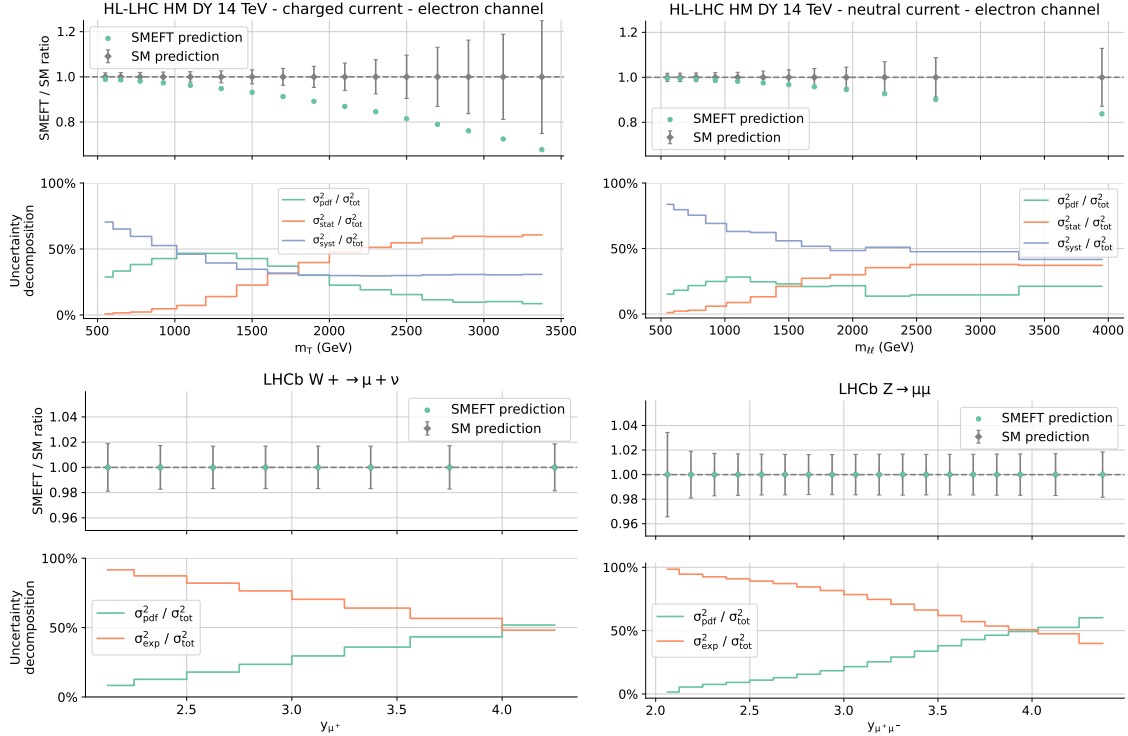


**Figure 3.3.** Projected impact of a flavour universal  $W'$  with  $m_{W'} = 13.8$  TeV ( $\hat{W} = 8 \times 10^{-5}$ ) on high-mass Drell–Yan (DY) distributions measured by ATLAS and CMS in the HL-LHC phase (top row) and in the forward bosons production measured by LHC in the HL-LHC phase (bottom row) for charged current DY (left column) and neutral current DY (right column). The BSM signal is compared to the SM prediction and its total uncertainty, which is split into component due to PDF uncertainty and a component due to experimental uncertainties in the lower insets. In the case of high-mass DY the experimental uncertainty is split into a statistic and a systematic components, while in the case of forward DY distributions the statistic uncertainty is subdominant and is not displayed separately.

other hand distortion effects associated to this model are very suppressed in the HL-LHC on-shell LHCb forward Drell-Yan measurements, as shown in the bottom row of Fig. 3.3, as the SMEFT predictions sit on top of the SM predictions, which in turn are dominated by systematic experimental uncertainties, apart from the most forward bins in which the PDF uncertainty becomes comparable to the experimental one.

In Fig. 3.4, we show that a fit of the  $\hat{W}$  Wilson coefficient can yield completely unreliable results if *BSM-biased* PDFs are used as input in the SMEFT fit. When the correct *true* PDFs are employed instead, the injected *true* value of  $\hat{W}$  is accurately recovered, differing from the SM expectation by more than  $5\sigma$ . By contrast, using a BSM-biased PDF set in the SMEFT fit leads to an apparent compatibility with the SM, while simultaneously excluding the *true* underlying theory with a significance exceeding  $5\sigma$ . This behaviour qualitatively reproduces the pattern already observed in the toy-model study shown in Fig. 2.1.

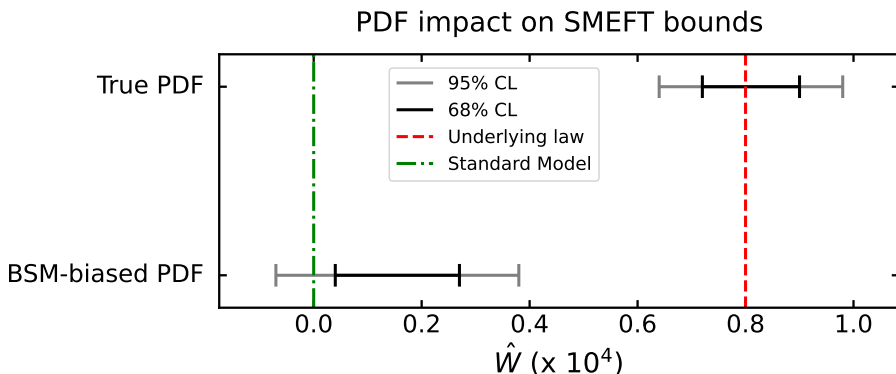


**Figure 3.4.** SMEFT fit performed on the synthetic Drell-Yan high-mass data and HL-LHC pseudodata presented in Sect. 3.1 with  $\hat{W} = 8 \times 10^{-5}$  injected. The 95% C.L. (grey) and 68% C.L. bands are displayed for a SMEFT fit in which the *true* PDFs are used as input set (top) and a fit in which the *BSM-biased* PDFs are used (bottom).

We now assess a set of strategies aimed at mitigating this undesirable behaviour and achieving a more robust determination of both PDFs and SMEFT coefficients, following the prescriptions outlined in Sect. 2.2. First, we perform a conservative PDF fit in which all high-mass Drell-Yan observables are excluded, and we subsequently use the resulting PDF set as input to a SMEFT fit. Second, we carry out a fully simultaneous fit of the PDFs and SMEFT coefficients.

To ensure the generality of our conclusions and to test the ability of these approaches to disentangle correlated effects, we generate synthetic data assuming an underlying scenario in which both  $\hat{W}$  and  $\hat{Y}$  are non-zero. We retain the same value of  $\hat{W} = 8 \cdot 10^{-5}$  as before and additionally inject  $\hat{Y} = 1.5 \times 10^{-4}$ , corresponding to an additional  $Z'$  with mass  $M_{Z'} = 18.7$  TeV. The resulting SMEFT constraints are shown in Fig. 3.5, while the corresponding PDF luminosities are presented in Fig. 3.6.

The SMEFT bounds shown in Fig. 3.5 demonstrate that both the simultaneous fit and the conservative fixed-PDF SMEFT fit successfully recover the underlying theory and clearly exclude the SM, in contrast to the BSM-biased fixed-PDF SMEFT fit. This be-

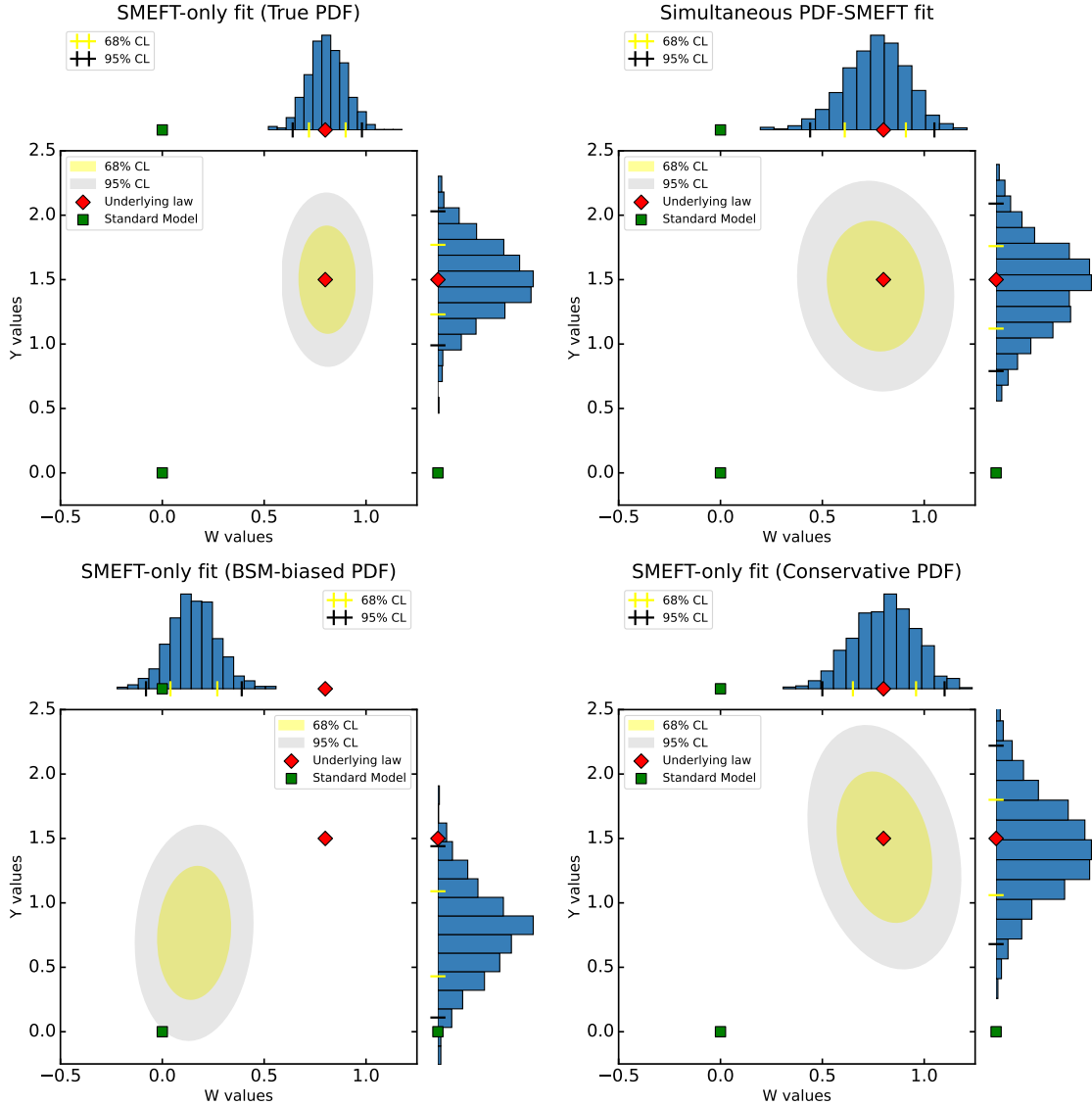


**Figure 3.5.** Comparison of SMEFT fits alongside the  $\hat{W}$  and  $\hat{Y}$  directions on Drell-Yan observables whose underlying law is  $\hat{W} = 8 \times 10^{-5}$  and  $\hat{Y} = 1.5 \times 10^{-4}$ . Upper left: Fixed-PDF SMEFT fit using the true PDFs used to generate the pseudodata. Bottom left: Fixed-PDF SMEFT fit using BSM-biased PDFs. Upper right: Simultaneous fit of the SMEFT and PDFs. Bottom right: Fixed-PDF fit using the conservative PDFs.

haviour closely mirrors that observed in the toy-model study presented in Fig. 2.1. For comparison, we also perform a fixed-PDF SMEFT fit using the true PDF set constrained by the full dataset. Although this does not represent a realistic scenario – since such PDFs are not accessible in practice – it provides an idealised benchmark corresponding to the best achievable constraints on the SMEFT coefficients. As expected, both the simultaneous and conservative fits yield wider uncertainties than this true fixed-PDF reference. The origin of the uncertainty broadening differs between the two approaches. In the conservative fit, the

looser SMEFT bounds arise directly from the increased PDF uncertainties in the large- $x$  region, which result from the removal of high-mass data that otherwise constrain large- $x$  quark and antiquark distributions. In the simultaneous fit, by contrast, the dataset is identical to that of the reference fit; the broader uncertainties instead reflect the much larger number of fitted parameters. In addition to the two SMEFT degrees of freedom, the fit simultaneously optimises the hundreds of parameters of the NNPDF parametrisation. Despite this significant increase in model complexity, the resulting uncertainty bands remain well under control. This indicates that the available dataset is sufficiently constraining to disentangle the marginal distributions of the SMEFT coefficients and the PDFs. We further observe that the correlation between  $\hat{W}$  and  $\hat{Y}$  is better reproduced in the simultaneous fit than in the conservative fit. Numerical values for the SMEFT confidence interval (CI) marginal bounds and the corresponding change in the  $\chi^2$  (compute on all experimental points that are sensitive to  $\hat{W}$  and  $\hat{Y}$  are reported in Tab. 3.4. We observe there that the marginalised bounds on the  $\hat{W}$  parameter are slightly tighter for the conservative than for the simultaneous one, while it is the opposite for the  $\hat{Y}$  parameter. As far as the

Fit	$\hat{W} \times 10^4$	$\hat{Y} \times 10^4$	$\Delta\chi^2$
True PDF	[0.64, 0.98]	[0.99, 2.03]	-
BSM-biased PDF	[-0.08, 0.39]	[0.11, 1.44]	+32 (+48)
Conservative PDF	[0.50, 1.10]	[0.68, 2.22]	-0.1 (+0.0)
Simultaneous fit	[0.44, 1.05]	[0.79, 2.09]	-0.7 (-1.0)

**Table 3.4.** Statistical summary of the  $\hat{W}$  and  $\hat{Y}$  fits to Drell–Yan observables shown in Fig. 3.5. The quoted bounds should be compared to the injected BSM signal used to generate the synthetic data, corresponding to  $\hat{W} = 8 \times 10^{-5}$  and  $\hat{Y} = 1.5 \times 10^{-4}$ . For each fit we show the 95% confidence interval (CI) marginal bounds on the  $\hat{W}$  and  $\hat{Y}$  fits obtained using different input PDFs and how much the total  $\chi^2$  (computed over all data-points included in the PDF fits,  $N_{\text{dat}} = 4363$ ) improves/deteriorates with respect to the baseline closure test in which the *true* PDFs are used as an input including or excluding (in brackets) the PDF uncertainty in the computation of the  $\chi^2$ .

global  $\chi^2$  is concerned, we observe that the global  $\chi^2$  is basically unchanged with respect to the baseline if conservative PDFs or if the PDFs obtained from a simultaneous PDF and SMEFT fit are used. On the other hand, if the BSM-biased PDF are used the global  $\chi^2$  deteriorates only marginally, less than  $0.5\sigma$  away, compared to the baseline, hence making the datasets with new physics injected look compatible with the SM.

In Fig. 3.6 we present the  $u\bar{d} + d\bar{u}$  PDF luminosity – which is mostly relevant for the charged–current Drell–Yan observables. The corresponding  $u\bar{u} + d\bar{d}$  luminosity for the neutral–current channel exhibits a very similar behaviour. We observe that the BSM–biased PDF luminosity effectively absorbs the energy–growing BSM signal present in the synthetic data (with BSM injected) shown in Fig. 3.3, thereby failing to reproduce the true underlying PDF law. This mechanism is responsible for the bias observed in the SMEFT analyses, which consequently appear compatible with the SM. In contrast, both the simultaneous and conservative PDF determinations robustly recover the underlying law, with comparable uncertainty bands.

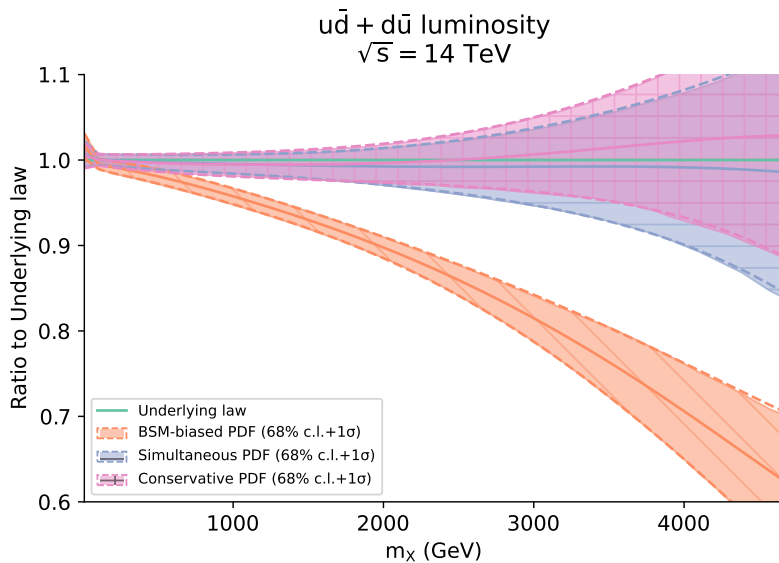


**Figure 3.6.** Comparison between the  $u\bar{d} + d\bar{u}$  PDF luminosities defined in this section and the *true* PDFs of the underlying law: the PDF luminosity obtained in a conservative fit, where all the high-mass Drell-Yan data are excluded (pink), the PDF luminosity obtained in a simultaneous fit of the PDFs with the SMEFT  $\hat{W}$  and  $\hat{Y}$  coefficients (blue) and the PDF luminosity obtained assuming the SM, hence BSM-biased (in orange). The error bands represent the 68% C. L. uncertainty of the resulting PDFs.

To summarise, we have shown that, in this case, both the simultaneous fit of PDFs and SMEFT coefficients and the conservative fixed-PDF SMEFT fit are able to disentangle the PDF–SMEFT mixing in the Drell–Yan sector first identified in [4]. Within the scope of this study, neither approach appears to outperform the other. It is worth noting, however, that the conservative PDFs could be safely trained by excluding only the high-mass Drell–Yan observables. In scenarios where additional sectors must be regarded as not “SM-safe” and consequently removed from the PDF fit, the performance of the conservative approach would likely deteriorate, whereas the simultaneous fit would remain largely unaffected.

### 3.3 BSM and PDF interplay in the top sector

In this section, we assess for the first time in the literature whether a BSM-induced bias may appear when the top data included in a PDF fit feature signs of new physics. In this case the gluon PDFs in the large- $x$  region could potentially absorb such signs. Like the large- $x$  anti-quark, the large- $x$  gluon is poorly constrained by pre-LHC data and its knowledge heavily relies on LHC data that are measured at large energy scale  $Q$  and/or large rapidity  $y$ . The strongest constraints come from high- $p_T$  inclusive jets, high invariant mass dijets, and the tails of the  $t\bar{t}$  invariant mass distributions [51–53]. If there was a BSM model producing energy-growing effects on such distributions, the effect could be possibly mimicked and absorbed by the gluon. Here we focus on the top sector, excluding the jet data from the input dataset for our PDF and SMEFT fits, leaving the latter to future studies [16, 17].

The model that we explore here is the  $\hat{Z}$  parameter, which belongs to the class of so-called *universal theories* [54]. It arises from the dimension-6 SMEFT matching of the Coloron model [55, 56], featuring a massive  $SU(3)_c$  color-octet vector field. A detailed description of the UV and SMEFT models is provided in App. A.3.

In order to assess whether the gluon PDF can absorb signs of such BSM model, we replicate the study of Ref. [11] in the  $\hat{Z}$  scenario. We inject several non-zero values of the  $\hat{Z}$  parameter in top invariant-mass distributions and identify what is the largest value of  $\hat{Z}$ , corresponding to the strongest BSM-induced deviation, which can be absorbed in the gluon PDF *without* visibly worsening the fit quality of the data as compared to the baseline SM fit. A poor fit quality would indicate that the data are not consistent with the SM predictions, and point out the possible presence of NP in them. We use the NNPDF criteria to tag a dataset as inconsistent, namely  $\chi^2 \geq 1.5$  and  $n_\sigma \geq 2$  [34]. We find that the threshold for maximal absorption of the NP signal in the gluon PDF is  $\hat{Z} = 4 \times 10^{-4}$ . In the UV Coloron model such a value of  $\hat{Z}$  corresponds to a coupling of  $g_G = 2$  and  $\alpha_G = g_G^2/4\pi \leq 1$  and  $M_G = 8.5$  TeV, which is large enough for the EFT approach to be valid even in the highest energy bins of the HL-LHC  $t\bar{t}$  pseudo-data that we consider here.

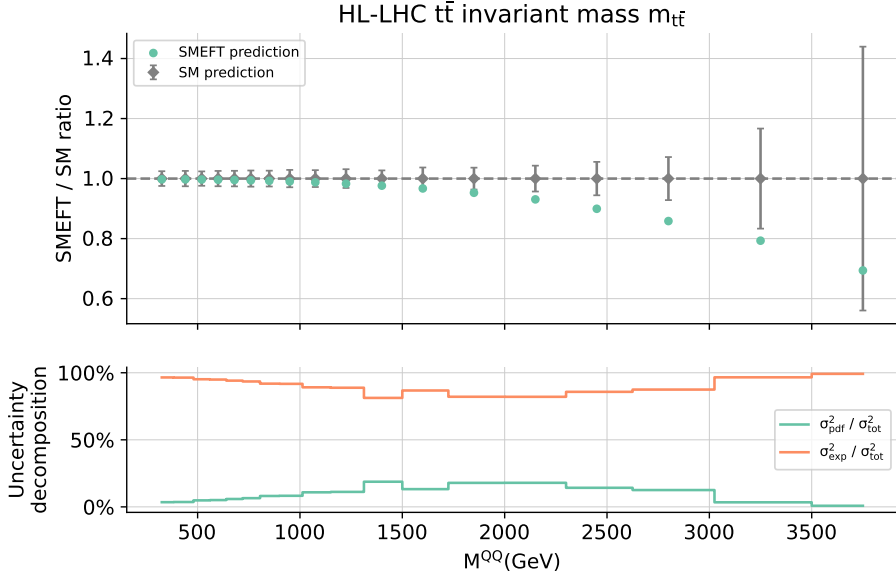


**Figure 3.7.** Same as Fig. 3.3, here showing the impact of the  $\hat{Z} = 4 \times 10^{-4}$  model on the HL-LHC projection for the  $t\bar{t}$  invariant mass distribution.

In the top-quark sector, in addition to the inclusive and differential  $t\bar{t}$  cross sections and  $t$ -channel single-top production already included in NNPDF4.0, we incorporate the additional observables introduced in Ref. [10]. These include  $t\bar{t}$  production asymmetries,  $W$ -boson helicity fractions, associated top-pair production with electroweak gauge bosons and heavy quarks—such as  $t\bar{t}Z$ ,  $t\bar{t}W$ ,  $t\bar{t}\gamma$ ,  $t\bar{t}t\bar{t}$ , and  $t\bar{t}b\bar{b}$ —as well as  $s$ -channel single-top production and associated single-top plus vector-boson processes. A non-zero value of  $\hat{Z}$  would affect all these distributions in the high-invariant mass bins, but the effect is enhanced in the HL-LHC scenario that we consider in our work. The impact on the

$t\bar{t}$  projections at the HL-LHC binned in the invariant mass of the top pair is displayed in Fig. 3.7. We see that the effect remains below 10% until the top pair invariant mass reaches 2 TeV, beyond which the impact reaches the 20-30% level exceeding the PDF uncertainty.

We fit the PDFs on the synthetic data presented in Sect. 3.1 – excluding all jets and dijets distributions – injecting the BSM signal in the data and assuming the SM in our theory prediction. For  $\hat{Z} = 4 \times 10^{-4}$  we obtain a fit-quality that is statistically equivalent to the fit performed on SM synthetic data using a SM theory, thus indicating that the BSM signal gets absorbed by the PDFs. The effect on the gluon-gluon luminosity is visible in Fig. 3.8, where we see that the gluon luminosity (pink) is mimicking the new physics signature present in the data and fails to recover the underlying law. In comparison both

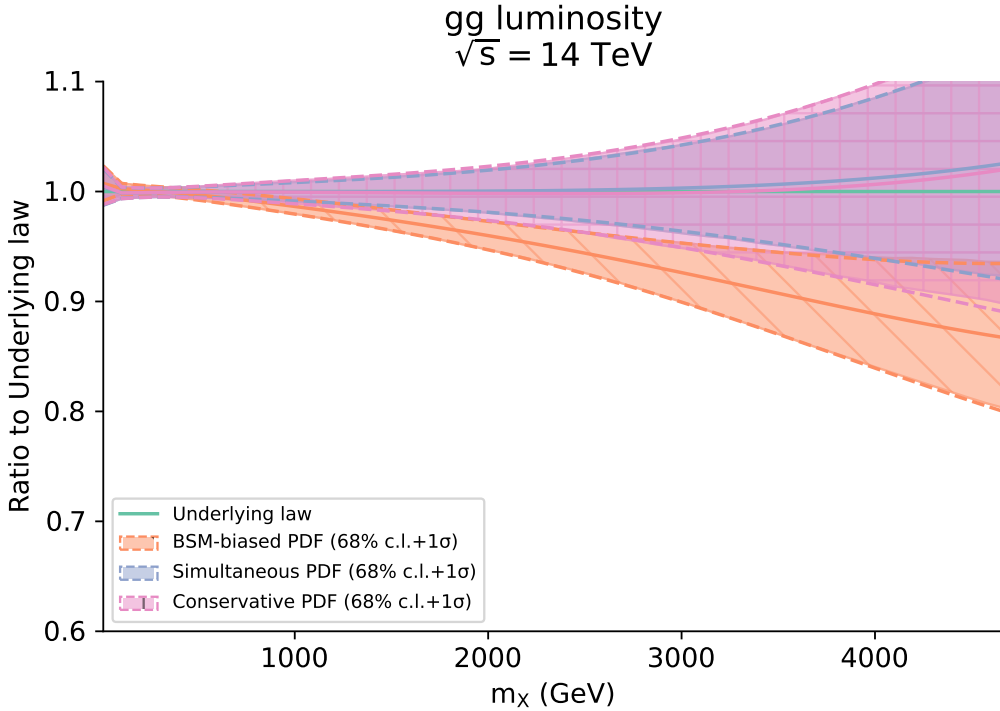


**Figure 3.8.** The *true* baseline gluon-gluon luminosity at  $\sqrt{s} = 14$  TeV in the central rapidity region (green line) is compared to the BSM-biased luminosity (orange) obtained by fitting synthetic data in which  $\hat{Z} = 4 \times 10^{-4}$  has been injected by assuming the SM, to a conservative luminosity (pink) obtained by excluding all top data from the PDF fit and to the result of a simultaneous fit of PDFs and SMEFT Wilson coefficients (blue). The results are normalised to the baseline SM luminosities and the 68% C.L. bands are displayed.

the conservative PDFs in which all high-mass top observables are excluded and the result of a simultaneous fit of PDF and SMEFT recover the underlying law. The PDF uncertainty bands associated with the conservative fit is systematically larger than the uncertainty of the PDFs obtained in a the simultaneous fit. The difference increases with the energy scale.

Finally, in Fig. 3.9 and Table 3.5 we compare the bounds on the  $\hat{Z}$  Wilson coefficient obtained using: the *true* PDF input set; the BSM-biased PDFs, the conservative PDFs and the SMEFT-PDF from a simultaneous fit of the PDFs and  $\hat{Z}$ . Again, using the *true* PDF,

we are able to clearly spot a deviation with respect to the SM. Inputting the BSM-biased PDF, we see that the absorption of NP signals in the gluon PDFs is only partial since we are not excluding the true underlying law, contrarily to what we observe in the DY sector. Instead, we obtain SMEFT bounds somewhat compatible with both the SM and the true BSM model. The result of the mixing between PDF and SMEFT is a somewhat

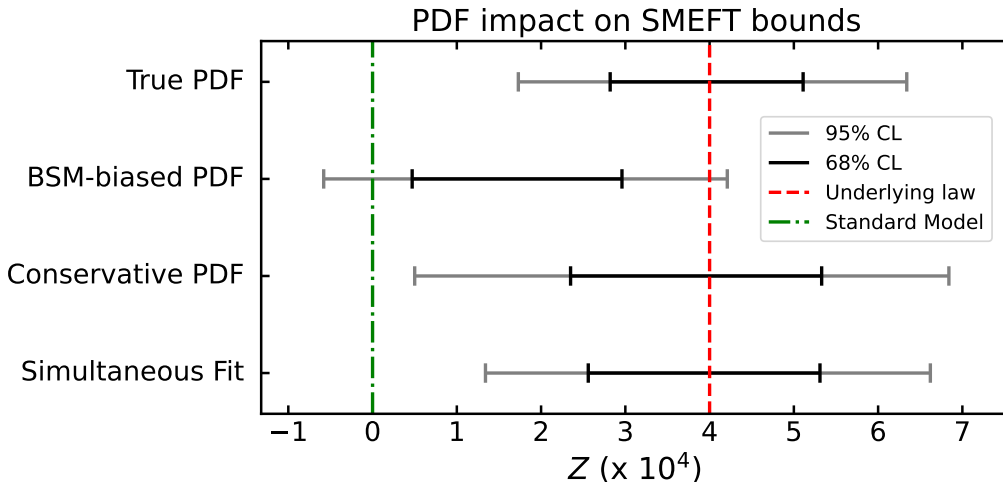


**Figure 3.9.** SMEFT fit performed on the  $t\bar{t}$  productions pseudodata mirroring existing measurements and augmented by HL-LHC projections, presented in Sect 3.1, with  $\hat{Z} = 4 \times 10^{-4}$  injected. The 95% (grey) and 68% (black) C.L. correspond to SMEFT fits using different PDF sets as inputs and to a simultaneous determination of PDFs and SMEFT.

watering down the deviation from the SM, from  $n_\sigma = 3.43$  to  $n_\sigma = 1.41$ . On the other hand the conservative fixed-PDF SMEFT fit and the simultaneous fit are both able to recover robustly the injected value of  $\hat{Z}$ . However, this time the simultaneous fit produces noticeably tighter bounds as compared to the bounds obtained by using *conservative* PDFs. This means that the benefit of being able to use the  $t\bar{t}$  observables binned in the invariant mass to constrain the gluon PDF outweigh the uncertainty increase due to fitting the PDF degrees of freedom alongside the SMEFT.

Fit	$\hat{Z} \times 10^4$	$\Delta\chi^2$
True PDF	[1.73, 5.11]	-
BSM-biased PDF	[-0.58, 4.21]	+5.1 (+6.4)
Conservative PDF	[0.50, 6.84]	+0.1 (+0.2)
Simultaneous fit	[1.34, 6.62]	+0.0 (+0.0)

**Table 3.5.** Same as Table 3.4, now for the  $\hat{Z}$  fits to top observables shown in Fig. 3.9. The quoted bounds should be compared to the injected BSM signal used to generate the synthetic data, corresponding to  $\hat{Z} = 4 \times 10^{-4}$ .

To conclude, we have shown that the risk of absorbing signs of new physics inside the

PDFs is not limited to the DY sector and the  $\hat{W}$  model, as it can also happen in the top quark sector. Thus, even if it appears to be a model and sector dependent effect since we only observed a partial absorption in the top sector while it was a total one for DY, we can assume that this risk is quite general and must be taken into account for robust SMEFT analyses. Once again, we have shown that both simultaneous and conservative fits are able to break the degeneracy between the PDF and the SMEFT.

## 4 Practical recommendations

In this section, we provide practical recommendations to identify a degeneracy between PDFs and potential signs of new physics. As we saw in Sect. 3, the fit quality of a BSM-biased PDF can be as good as the one of a consistent fit, both in the DY and in the top sector. This makes it difficult to distinguish between the two without prior knowledge of the true underlying law. In this section we explore two approaches that can be used in real life – where the underlying BSM model is unknown – to identify possible PDF-induced bias. In Sect. 4.1, we explore model-agnostic conservative PDF fits, while in Sect. 4.2, we discuss more in depth the nature of the degeneracy between the NP signals, which scales with energy, and the PDFs, which depend on the Bjorken  $x$  and design a set of ratio observables at different centre-of-mass energies that could disentangle NP signals and PDF effects.

### 4.1 Implementing energy cut-offs

In Sect. 3, we performed SMEFT fits by using some *ad-hoc* conservative PDFs that we produced by removing from the global PDF analysis all the data affected by the *known* BSM model that we were injecting in the synthetic data. In particular, in the case of Drell-Yan we removed all high invariant and transverse masses DY distributions, while in the case of top we removed all high-invariant mass distributions.

In realistic scenarios, where the specific BSM dynamics responsible for potential distortions in the high-energy tails of measured distributions are unknown, it is generally unclear which datasets should be excluded in order to construct a conservative PDF fit free from BSM-induced biases. In this section, we adopt an agnostic strategy in which conservative PDF sets are obtained by performing fits that exclude all data above a given energy threshold,  $Q_{\max}$ . This approach exploits the fact that SMEFT-induced deviations typically grow with energy, allowing us to identify characteristic signatures in both the PDFs and the SMEFT constraints obtained using conservative PDFs as input sets. If PDFs are effectively absorbing BSM-induced deviations in the observables, varying the energy cut is expected to modify these distortions in a way that renders the corresponding PDF fits mutually incompatible. By contrast, in the SM (baseline) case, the universality of PDFs implies that fits performed with different energy thresholds should remain consistent, with only an increase in uncertainties as higher-energy data are progressively removed. We therefore expect the uncertainty bands to broaden as  $Q_{\max}$  is lowered and the available dataset is reduced. One should be aware that if the energy cuts become too restrictive, extrapolation

effects may lead to spurious behaviour, as insufficient data remain to constrain the PDFs in the large- $x$  region.

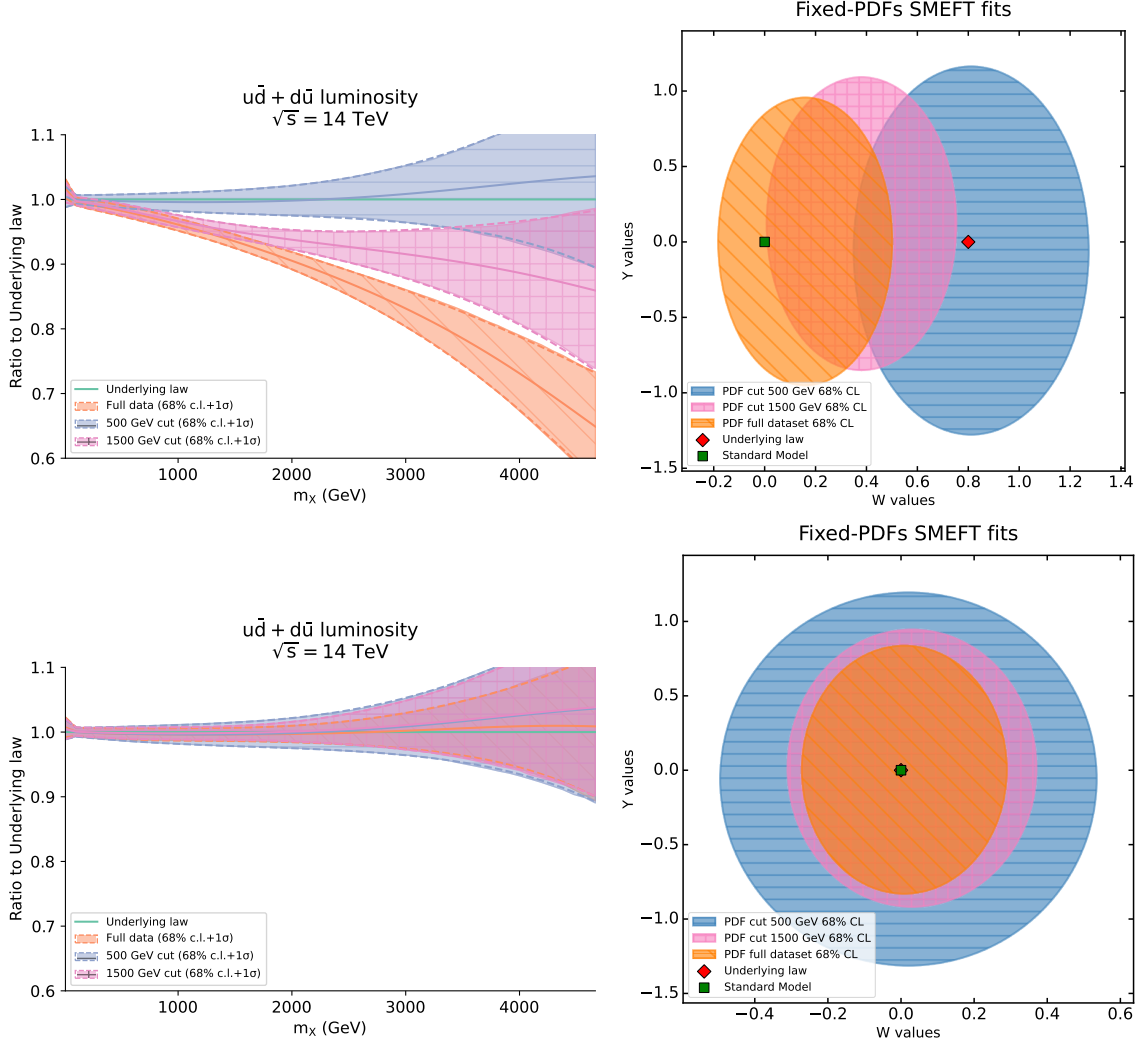


**Figure 4.1.** Impact of various energy cut  $Q_{\max}$  in the input PDF sets. In the top row all synthetic data were generated by injecting the BSM model discussed in Sect. 3.2 (corresponding to  $\hat{W} = 8 \cdot 10^{-5}$ ). In the bottom row the synthetic data were generated assuming the SM. On the left panels the relevant PDF luminosities  $u\bar{d} + \bar{u}d$  obtained by varying  $Q_{\max}$  are compared in the two cases. On the right panels the SMEFT bounds obtained in a SMEFT-only fit by using the PDFs with different  $Q_{\max}$  as an input are compared.

We test this model-agnostic diagnostic strategy in the Drell–Yan scenario discussed in Sect. 3.2, with  $\hat{W} = 8 \times 10^{-5}$ , for which both the injected BSM signal and the resulting PDF bias are known. Figure 4.1 illustrates the impact of imposing global energy cuts at  $Q_{\max} = 500$  and 1500 GeV on the extracted PDFs and on the corresponding SMEFT fits obtained using these conservative PDF sets as an input. In the top panel, where the synthetic data include a BSM contribution, we observe that imposing a very conservative cut of  $Q_{\max} = 500$  GeV (blue band) completely removes the bias present when the full

dataset is used (orange band), thereby restoring the correct underlying theory. By contrast, a milder cut at  $Q_{\max} = 1500$  GeV (pink band) is insufficient to eliminate the contamination. The progressive departure from the underlying law as increasingly NP-sensitive data are included is clearly visible. Such behaviour would not arise if the data were generated consistently within the SM, as illustrated in the bottom panel. As expected, the PDF uncertainty bands broaden as  $Q_{\max}$  is lowered and more data are excluded from the fit. A similar pattern emerges in the SMEFT-only analyses performed using the increasingly conservative PDF sets, shown in the right panel. The SMEFT bounds obtained with the  $Q_{\max} = 500$  GeV PDFs are well centred on the underlying BSM value, albeit with substantially larger uncertainties. As the energy cut is relaxed, the bounds progressively shift towards the SM—ultimately excluding the correct BSM scenario—while becoming increasingly stringent. Finally, in the bottom panels of Fig. 4.1, we show that when the synthetic data are generated within the SM, the SMEFT bounds remain centred on the true values as  $Q_{\max}$  is varied, with only a gradual increase in the uncertainties as higher-energy data are removed.

SMEFT Fit using	SM data	BSM data	$N_{\text{points}}$
No cut	—	20.9	4363
$Q_{\max} = 1500$ GeV	-1.1	13.2	4339
$Q_{\max} = 500$ GeV	-1.00	-1.2	4262

**Table 4.1.** Total  $\Delta\chi^2$  of the SMEFT fits presented on the right panels of Fig. 4.1 computed using fixed PDF sets trained on datasets cut at different values of  $Q_{\max}$ . Results are shown for fits to SM synthetic data and data with BSM signal injected (corresponding to  $\hat{W} = 8 \times 10^{-5}$ ).

In Table 4.1, we report the variation in the global fit quality,  $\Delta\chi^2 = \chi_{\text{fit}}^2 - \chi_{\text{baseline}}^2$ , obtained using the different PDF sets constructed by imposing a maximum energy cut  $Q_{\max}$ . The baseline reference corresponds, as usual, to the fit of SM synthetic data using SM predictions. Two distinct patterns emerge when comparing fits performed on synthetic data generated within the SM to those obtained from data containing an injected BSM signal. In the SM case, the choice of  $Q_{\max}$  has essentially no impact on the fit quality. This behaviour is expected, since all datasets are mutually consistent by construction, being generated from the same underlying theory. By contrast, for synthetic data generated with an injected  $\hat{W} = 8 \times 10^{-5}$  signal, the fit performed without any high-energy cuts exhibits an increase in the global  $\chi^2$  of about 21 units, indicating a mild tension. When an energy cut at 1500 GeV are imposed, the corresponding  $\Delta\chi^2$  values decrease progressively, but remain positive. This behaviour can be understood from the top-left panel of Fig. 4.1: as the energy cut becomes more stringent, the PDF luminosity approaches the underlying law, yet still fails to reproduce it accurately. This reflects the fact that neither cut is sufficient to fully remove the BSM contamination present in the HL-LHC dataset. In contrast, the  $Q_{\max} = 500$  GeV cut successfully eliminates the residual BSM contribution. As a result, the associated PDF and SMEFT fits robustly recover the underlying theory, and the corresponding fit quality becomes comparable to that of the baseline case.

In summary, this relatively simple diagnostic test can be used to assess the risk that energy-growing deviations are being absorbed into the PDFs. A progressive shift of the type observed in Fig. 4.1 would act as warning signal, indicating the presence of potential inconsistencies associated with energy-dependent effects, and hence possibly of BSM origin, in the dataset used for the PDF fit. Such behaviour would motivate the adoption of a conservative  $Q_{\max}$  cut in order to ensure a robust and unbiased PDF determination.

## 4.2 Breaking Bjorken- $x$ and $M^2$ degeneracy

A second approach to identify a potential BSM-bias in the PDFs is to use test observables not present in the fit which break the degeneracy between the PDF and the SMEFT behaviour. In the case of a proton-proton collision producing a final state  $A$ , where  $A$  could be for example a DY pair or a  $t\bar{t}$  pair, collinear factorisation yields, up to power suppressed terms:

$$\sigma_{\text{pp}\rightarrow A}(M^2) = \sum_{ij} \int dx_1 dx_2 f_i^{(1)}(x_1, \mu) f_j^{(2)}(x_2, \mu) \hat{\sigma}_{ij\rightarrow A}(M^2, \mu), \quad (4.1)$$

where  $f_i^{(1)}$  and  $f_j^{(2)}$  are the PDFs of the two incoming protons,  $x_1$  and  $x_2$  are the Björken- $x$  of the partons involved in the perturbative interaction ( $ij \rightarrow A$ ),  $M$  is the invariant mass of the final states produced in the hard scattering collision, and  $\mu$  collectively indicate the factorisation and renormalisation scales of the process.

At tree level, since  $x_1$  and  $x_2$  correspond to the fraction of the momentum of the protons carried by the partons, conservation of energy simply yields

$$M^2 = x_1 x_2 s, \quad (4.2)$$

where  $\sqrt{s}$  is the centre-of-mass energy of the proton-proton collision.

The main point here is that the SMEFT effects grow with the energy scale  $M$ . The linear corrections stemming from dim-6 four fermion operators grow with  $M^2/\Lambda^2$ , where  $\Lambda$  is around the scale of the new physics, where the SMEFT expansion breaks. On the other hand, PDFs depend on  $x$ . The observed BSM-induced bias in the PDFs corresponds to a degeneracy between the  $x$  and  $M^2$  dependencies of the observables described in Eq. 4.1 at a given centre-of-mass energy. If  $\sqrt{s}$  changes, the same  $M^2$  bin would correspond to different Bjorken- $x$  values. The argument on the dependence of the PDFs on the  $M^2/s$  ratio has been considered in Ref. [57], where examples of cross section ratios taken at different centre-of-mass energies were considered and their implication in terms of precision SM measurements was discussed.

In Fig. 4.2, we compare the  $u\bar{u} + d\bar{d}$  parton luminosities obtained from the same BSM-biased PDF set, which mimics the deviations induced by a  $\hat{W} = 8 \times 10^{-5}$  scenario in high-mass Drell-Yan observables at  $\sqrt{s} = 14$  TeV, as discussed in Sect. 3.2. We show the ratios of these luminosities at different hadronic centre-of-mass energies, namely  $\sqrt{s} = 9, 14, \text{ and } 20$  TeV, to the corresponding underlying law derived from SM synthetic data and SM theoretical predictions. The choices of 9 and 20 TeV are not motivated by specific

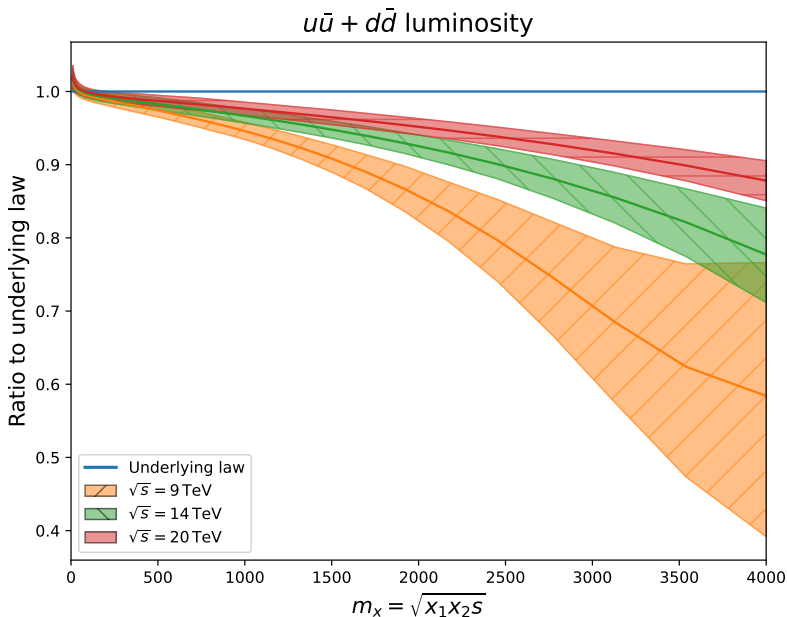


**Figure 4.2.** Ratio of the  $u\bar{u} + d\bar{d}$  parton luminosity at different centre-of-mass energies with respect to the underlying law. The input PDF set is given by the BSM-biased PDF mimicking the deviations caused by  $\hat{W} = 8 \times 10^{-5}$  model in high-mass Drell–Yan observables at  $\sqrt{s} = 14$  TeV, discussed in Sect. 3.2.

experimental proposals, but are adopted here for illustrative purposes, in order to demonstrate how varying  $\sqrt{s}$  can help break the degeneracy between the partonic momentum fractions and the invariant mass.

We observe that the BSM-mimicking deviation, which develops from observables measured at  $\sqrt{s} = 14$  TeV, exhibits a pronounced dependence on the hadronic centre-of-mass energy. As  $\sqrt{s}$  decreases, the deviation from the underlying law increases for fixed values of  $M^2 = x_1 x_2 s$ , while the opposite trend is observed when  $\sqrt{s}$  is increased. This behaviour can be understood from simple kinematic considerations. For a smaller centre-of-mass energy, for instance  $\sqrt{s_{\text{small}}} = 9$  TeV compared to  $\sqrt{s_{\text{large}}} = 14$  TeV, the partonic momentum fractions corresponding to a given invariant mass  $M$  are larger, since  $x_1 x_2 = M^2/s$ , namely

$$\frac{M^2}{s_{\text{small}}} = x_1^{(s_{\text{small}})} x_2^{(s_{\text{small}})} > x_1^{(s_{\text{large}})} x_2^{(s_{\text{large}})} = \frac{M^2}{s_{\text{large}}} \quad , \quad \text{for fixed } M. \quad (4.3)$$

Conversely, for fixed values of  $x_1 x_2$ , the corresponding invariant mass rescales with the hadronic centre-of-mass energy as

$$M^2(s) = x_1 x_2 s \quad \Rightarrow \quad M^2(s_{\text{large}}) = M^2(s_{\text{small}}) \frac{s_{\text{large}}}{s_{\text{small}}} \quad , \quad \text{for fixed } x_1 x_2. \quad (4.4)$$

This feature can be exploited to construct test observables at centre-of-mass energies different from those used in the PDF fit. In Fig. 4.3, we show the ratio of BSM Drell–Yan projections at the HL-LHC to the corresponding SM predictions, evaluated using both the true PDFs and the BSM-biased ones. We present leading-order projections for

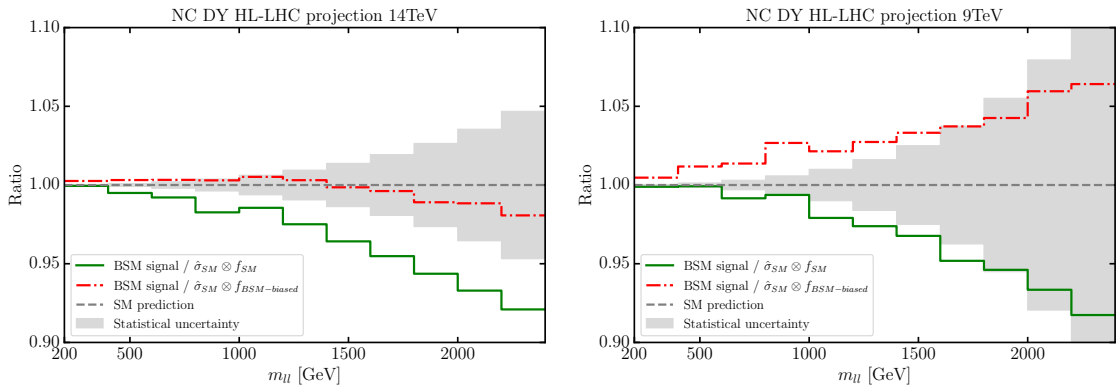


**Figure 4.3.** Predictions for NC DY ( $pp \rightarrow l^-l^+$ ) inclusive cross sections differential in  $M_{ll}$ , with  $l = (e, \mu)$  for  $\sqrt{s} = 14$  TeV (left) and  $\sqrt{s} = 9$  TeV (right). The BSM observables are compared to SM predictions using the true PDFs (green) and the BSM-biased PDFs (red).

$\sqrt{s} = 14$  TeV in the left panel and for  $\sqrt{s} = 9$  TeV in the right panel. For  $\sqrt{s} = 14$  TeV, the BSM-biased PDFs successfully mimic the genuine new-physics deviations, thereby making the observables appear spuriously consistent with the SM, whereas a clear discrepancy is visible when using the true PDFs. For  $\sqrt{s} = 9$  TeV, the SMEFT-induced deviations remain unchanged, as they depend only on the binning in the invariant mass  $m_{\ell\ell}^2$ . Consequently, the ratio of the BSM prediction to the SM expectation obtained with the true PDFs is unaffected. In contrast, the comparison based on the BSM-biased PDFs is no longer compatible with the SM. In this case, the PDFs overcompensate the SMEFT effects, as already illustrated in Fig. 4.2, leading to an apparent deviation from the SM in the *opposite direction* to the true one.

We note that, at  $\sqrt{s} = 9$  TeV, the number of events at large  $m_{\ell\ell}$  is significantly reduced compared to  $\sqrt{s} = 14$  TeV, resulting in larger statistical uncertainties in this region. For simplicity, we have assumed the full HL-LHC integrated luminosity for both centre-of-mass energies, although this does not correspond to a realistic experimental scenario. Nevertheless, realistic measurements can still disentangle PDF effects from SMEFT contributions. As shown in Ref. [12], deep-inelastic scattering data from the EIC [58] and measurements at the Forward Physics Facility [59] can help break this degeneracy. Other proposed experimental programmes, such as the LHeC [60], are expected to provide similar benefits. These measurements probe the same partonic channels as high-mass Drell–Yan processes, but at much higher rapidities, thereby breaking the alignment between  $x$  and  $M^2$  that characterises BSM-biased PDFs.

### 4.3 Comparing different sectors

A complementary strategy to disentangle PDF and SMEFT effects using test observables consists in exploiting the fact that different processes and kinematic sectors can be affected in qualitatively different ways by the same NP scenario. By comparing observables across such sectors, one can therefore construct powerful consistency tests that are sensitive to BSM contamination in PDF fits.

As a representative example, in Fig. 4.4 we show the impact of the  $\hat{Z} = 4 \times 10^{-4}$  scenario discussed in Sect. 3.3 on a dijet observable [61]. This measurement from ATLAS at  $\sqrt{s} = 13$  TeV is presented as double differential cross sections in the invariant mass of the 2-jet system,  $m_{12}$ , and the absolute rapidity separation  $|y^*|$  of the pair of jets in the 2-jet event. SM theory predictions for these distributions have been released [62] as APPLFAST interpolation grids on the PLOUGHSHARE website<sup>4</sup>. They have been computed using the NNLOJET parton level event generator [39]. In [63], the aforementioned grids were converted in the PINEAPPL format [64]. In contrast to the suppression of events in the  $t\bar{t}$  invariant-mass distribution, illustrated in Fig. 3.7, the injection of the  $\hat{Z}$  model in the dijet predictions produces an enhancement in the predicted event yield with respect to the SM expectation. This opposite response of the two sectors constitutes a highly non-trivial signature of the underlying BSM dynamics. To our knowledge, such a direct and systematic comparison between top-quark and jet observables as a diagnostic tool for PDF–BSM interplay has not been explored in previous studies. The fact that the same BSM scenario induces qualitatively different effects in these channels provides a novel and robust handle to test the consistency of PDF-based interpretations.

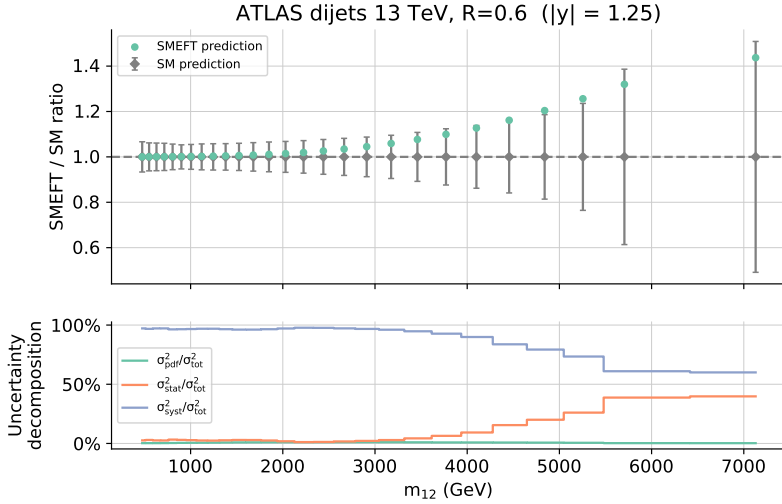


**Figure 4.4.** Top: Impact of the  $\hat{Z} = 4 \times 10^{-4}$  model on the dijet invariant mass  $m_{12}$  distribution in the  $1.0 < |y^*| < 1.5$  bin measured by the ATLAS collaboration [61]. Bottom: uncertainty decomposition in terms of PDF (green), statistical (orange) and systematic (blue) as ratio to the total uncertainty.

In the present case, dijet observables were not included in the PDF fit, whereas  $t\bar{t}$  data are. As a consequence, the BSM-biased PDFs absorb the suppression of high-energy events observed in the  $t\bar{t}$  channel and effectively encode a decreasing behaviour with energy. When such PDFs are subsequently used to analyse dijet distributions, they no longer mask the BSM effects. Instead, they amplify the discrepancy with respect to the SM prediction, as shown in Fig. 4.5, thereby revealing the underlying inconsistency.

<sup>4</sup><https://ploughshare.web.cern.ch/ploughshare>

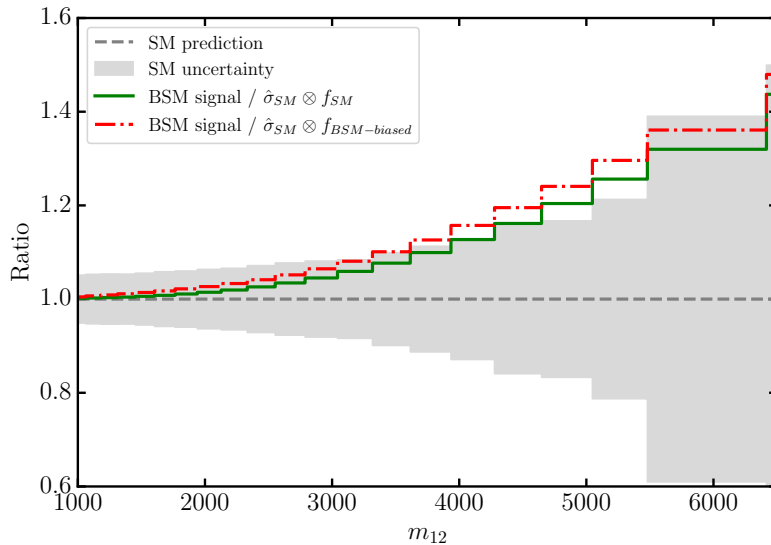


**Figure 4.5.** Predictions for dijet inclusive cross sections differential in the dijet invariant mass  $m_{12}$ . The BSM observables are compared to SM predictions using the true PDFs (green) and the BSM-biased PDFs (red).

More generally, in Ref. [11] we demonstrated that BSM-biased PDFs can also induce artificial deviations in processes involving the same partonic channels as high-mass Drell–Yan production, but which are not directly affected by the same SMEFT operators, such as  $WW$  production. Since these processes are measured at the same centre-of-mass energy, the PDF-induced distortions are comparable, while the SMEFT contributions differ. This mismatch leads to observable tensions that can be exploited as additional consistency checks.

Taken together, these examples illustrate that combining information from multiple sectors with distinct sensitivities to new physics provides a powerful means of disentangling PDF effects from genuine SMEFT contributions. While this strategy is intrinsically model dependent and requires a detailed understanding of how specific BSM scenarios impact different observables, it offers a valuable and largely unexplored avenue for improving the robustness of global BSM analyses.

## 5 Conclusions

To summarise, in this work we have investigated two complementary strategies to disentangle the mixing between PDFs and BSM effects first observed in Ref. [11], considering benchmark scenarios involving a new  $W'$  and  $Z'$  in the Drell–Yan sector, as well as a new  $G'$  boson in top-quark pair production. Both approaches proved successful in mitigating BSM-induced biases in PDF-based analyses. These consist of the use of *conservative* PDF fits, in which observables potentially affected by new physics are excluded by imposing an upper energy threshold  $Q_{\max}$ , and of fully *simultaneous* fits of PDFs and SMEFT coefficients.

Conservative fits constrain the PDFs under the assumption of the SM by relying, in principle, only on SM-safe measurements. The resulting PDFs are then used as input in a subsequent SMEFT analysis. The main limitation of this approach lies in the choice of an energy cut that is sufficiently conservative to suppress BSM-induced biases, while not being so restrictive as to excessively inflate PDF uncertainties, which are then propagated to the SMEFT fit. In Sect. 3, we have shown that, in the presence of  $W'$  and  $Z'$  contributions to Drell–Yan production, conservative fits yield constraints that are competitive with those obtained from simultaneous fits. By contrast, in the case of a  $G'$  affecting  $t\bar{t}$  production, conservative fits lead to visibly weaker bounds. This indicates that the performance of this strategy is intrinsically dependent on the underlying model and on the sector under consideration.

Simultaneous fits, on the other hand, make use of the full dataset to constrain both PDFs and SMEFT coefficients, without assuming the SM during the fitting procedure. In this way, potential BSM-induced distortions of the PDFs are absorbed into the extended parameter space rather than biasing the PDF determination. As a result of the substantially larger number of trainable parameters, simultaneous fits typically exhibit broader uncertainties than idealised SMEFT-only fits based on the true PDFs, which are not accessible in practice. Nevertheless, as demonstrated in both the Drell–Yan and  $t\bar{t}$  studies presented here, the inclusion of high-energy observables affected by BSM dynamics provides sufficient constraining power to compensate for this increase in dimensionality. In all scenarios considered, this approach proved effective in recovering both the PDFs and, most importantly, the underlying BSM dynamics.

It is important to stress, however, that simultaneous PDF–SMEFT fits cannot be straightforwardly extended to arbitrarily large operator bases, due to the rapidly increasing dimensionality of the parameter space and the associated computational and statistical challenges. In this respect, systematic strategies to identify the most relevant operators, such as those proposed in Ref. [65], play a crucial role in reducing the effective dimensionality of the problem and enabling scalable global analyses.

Finally, we have proposed three practical recommendations for identifying potential BSM-induced biases in PDF determinations, which can otherwise remain hidden, since the absorption of BSM effects does not necessarily lead to an observable deterioration of the fit quality. The first consists in performing PDF fits with different agnostic energy cuts and testing the mutual compatibility of the resulting PDFs and SMEFT constraints. Incompatibilities associated with energy-growing deviations may signal the presence of BSM contamination. Care must be taken, however, as excessively stringent cuts may induce spurious tensions through uncontrolled extrapolation in poorly constrained kinematic regions. The second recommendation is to exploit test observables measured at different centre-of-mass energies or in distinct rapidity ranges, thereby breaking the degeneracy between PDFs and BSM effects that exists at fixed kinematics. Finally, the third recommendation consists in devising test observables – not included in a PDF fit – so that combining information from different sectors with distinct sensitivities to new physics may enable us to disentangle PDF effects from genuine BSM contributions.

Overall, our results highlight the importance of systematically accounting for the in-

terplay between PDFs and SMEFT in global analyses aimed at indirect searches for new physics. The methodologies developed in this work have been validated through closure tests based on consistent fixed-order synthetic data. The continuous development of novel Machine Learning (ML) techniques applied to high energy physics [66] may provide additional tools to identify latent correlations between PDFs and SMEFT directions, and to construct optimised diagnostic observables.

A natural and important extension of this programme is the investigation of real experimental measurements that induce substantial shifts in PDF determinations, such as those in the jet sector, which is currently under active study. A further next step will be the application of these methods to full global PDF analyses based on real experimental data, including higher-order theoretical corrections. It will also be important to explore how these strategies can be integrated within PDF4LHC-style combinations and future community recommendations.

## Acknowledgments

We thank Fabio Maltoni and Michelangelo Mangano for useful discussions that inspired this work and for their comments that improved it. We are immensely grateful to James Moore, who gave a substantial contribution to shape the questions that we address here. E. H., M. N. C., and M. U. are supported by the European Research Council under the European Union’s Horizon 2020 research and innovation Programme (PBSP, Grant agreement n.950246). M. U. is partially supported by the STFC consolidated grant ST/X000664/1. E. H. is partially supported by the Swiss National Science Foundation. L. M. acknowledges support from the European Union under the MSCA fellowship (Grant agreement N. 101149078) Advancing global SMEFT fits in the LHC precision era (EFT4ward). E. C. is supported by Newnham College, Cambridge and by the STFC Centre for Doctoral Training (CDT) in Data Intensive Science. F. M. is supported by Swiss National Science Foundation (SNF) under grant number 200021-231259.

## A Description of the new physics scenarios

### A.1 The $W'$ model and the $\hat{W}$ parameter

We consider an extension of the SM by a heavy  $W'$  triplet transforming in the adjoint representation of  $SU(2)_L$  and coupling universally to left-handed fermions and the Higgs doublet. The full details of the model are provided in Sect. 3 of [11] and in [67]. The complete UV Lagrangian is:

$$\begin{aligned} \mathcal{L}_{\text{UV}}^{W'} = & \mathcal{L}_{\text{SM}} - \frac{1}{4} W'_{\mu\nu} W'^{a,\mu\nu} + \frac{1}{2} M_{W'}^2 W'^a W'^{a,\mu} \\ & - g_{W'} W'^{a,\mu} \sum_{f_L} \bar{f}_L T^a \gamma^\mu f_L - g_{W'} (W'^{a,\mu} \varphi^\dagger T^a i D_\mu \varphi + \text{h.c.}), \end{aligned} \quad (\text{A.1})$$

For masses  $M_{W'}$  greater than 10 TeV, we find that this model is well described by the dimension-6 SMEFT Lagrangian for the HMDY HL-LHC projections presented in Tab. 3.1. Furthermore, at the energies at which the BSM physics becomes relevant for the observables, the SMEFT four-fermion operators largely dominate the BSM contributions. Therefore, in practice, the relevant SMEFT Lagrangian used throughout this study is:

$$\mathcal{L}_{\text{SMEFT}}^{W'} = \mathcal{L}_{\text{SM}} - \frac{g_{W'}^2}{2M_{W'}^2} J_L^{a,\mu} J_{L,\mu}^a, \quad J_L^{a,\mu} = \sum_{f_L} \bar{f}_L T^a \gamma^\mu f_L. \quad (\text{A.2})$$

We can measure the strength of the BSM signal by using the  $\hat{W}$  dimensionless parameter:

$$\mathcal{L}_{\text{SMEFT}}^{W'} = \mathcal{L}_{\text{SM}} - \frac{g^2 \hat{W}}{2m_W^2} J_L^{a,\mu} J_{L,\mu}^a, \quad \hat{W} = \frac{g_{W'}^2}{g^2} \frac{m_W^2}{M_{W'}^2} \propto \mathcal{C}_{lq}^3 \text{ (Warsaw basis)}, \quad (\text{A.3})$$

where  $g$  and  $m_W$  are the SM  $W$  boson coupling and mass respectively. If we assume that  $g_{W'} = 1$ , we have a direct connection between  $\hat{W}$  and  $M_{W'}$ . The limit  $\hat{W} = 0$  corresponds to  $M_{W'} \rightarrow \infty$ , *i.e.* the SM limit. On the other hand, a greater value of  $\hat{W}$  corresponds to a lower mass of the  $W'$ , which would have a greater impact on the HL-LHC observables.

### A.2 The $Z'$ model and the $\hat{Y}$ parameter

Similarly, we consider a  $Z'$  field associated with a  $U(1)_Y$  interaction. The full details of the model are also provided in Sect. 3 of [11] and in [67]. It extends the SM Lagrangian by the UV terms:

$$\begin{aligned} \mathcal{L}_{\text{UV}}^{Z'} = & \mathcal{L}_{\text{SM}} - \frac{1}{4} Z'_{\mu\nu} Z'^{\mu\nu} + \frac{1}{2} M_{Z'}^2 Z'_\mu Z'^\mu \\ & - g_{Z'} Z'_\mu \sum_f Y_f \bar{f} \gamma^\mu f - Y_\varphi g_{Z'} (Z'_\mu \varphi^\dagger i D^\mu \varphi + \text{h.c.}). \end{aligned} \quad (\text{A.4})$$

As in the  $W'$  case, we can match it to the SMEFT provided that  $M_{Z'}$  is sufficiently larger than the experimental scale, which we have ensured throughout the study:

$$\mathcal{L}_{\text{SMEFT}}^{Z'} = \mathcal{L}_{\text{SM}} - \frac{g_{Z'}^2}{2M_{Z'}^2} J_Y^\mu J_{Y,\mu}, \quad J_Y^\mu = \sum_f Y_f \bar{f} \gamma^\mu f. \quad (\text{A.5})$$

The dimensionless oblique parameter  $\hat{Y}$  is used to describe the intensity of the new physics signal:

$$\mathcal{L}_{\text{SMEFT}}^{Z'} = \mathcal{L}_{\text{SM}} - \frac{g'^2 \hat{Y}}{2m_W^2} J_Y^\mu J_{Y,\mu}, \quad \hat{Y} = \frac{g_{Z'}^2}{M_{Z'}^2} \frac{m_W^2}{g'^2}. \quad (\text{A.6})$$

### A.3 The coloron model $\mathcal{G}$ and the $\hat{Z}$ parameter

Finally, we consider a massive  $\text{SU}(3)_c$  octet field  $\mathcal{G}_a^\mu$ , where  $a$  is the colour index associated with the generators of the adjoint representation of the  $\text{SU}(3)_c$  group. This is referred to as the *Coloron* model in the literature [55, 56]. This model was not explored in [11], we will therefore provide some more details about it here.

The Coloron has properties similar to those of the gluon, and we might improperly refer to it as a ‘heavy gluon’. It is assumed that it acquires its mass  $M_{\mathcal{G}}$  via a Higgs-like mechanism, which we do not discuss in detail. It couples to the  $\text{SU}(3)_c$  current similarly to what the gluon does with a coupling constant  $g_{\mathcal{G}}$ . The UV Lagrangian extension reads:

$$\mathcal{L}_{\text{UV}}^{\mathcal{G}} = \mathcal{L}_{\text{SM}} - \frac{1}{4} \mathcal{G}_{\mu\nu}^a \mathcal{G}^{a,\mu\nu} + \frac{1}{2} M_{\mathcal{G}}^2 \mathcal{G}_\mu^a \mathcal{G}^{a,\mu} - g_{\mathcal{G}} \mathcal{G}_\mu^a \sum_q \bar{q} \gamma^\mu T^a q, \quad (\text{A.7})$$

where  $q$  are the SM quarks, and  $T^a$  the generators of the fundamental representation of  $\text{SU}(3)_c$ . The field strength tensor reads

$$\mathcal{G}_{\mu\nu}^a = \partial_\mu \mathcal{G}_\nu^a - \partial_\nu \mathcal{G}_\mu^a + g_s f^{abc} \mathcal{G}_\mu^b \mathcal{G}_\nu^c. \quad (\text{A.8})$$

The matching of the UV complete Lagrangian  $\mathcal{L}_{\text{UV}} = \mathcal{L}_{\text{SM}} + \Delta\mathcal{L}_{\mathcal{G}}$ , where  $\Delta\mathcal{L}_{\mathcal{G}}$  is defined in Eq. A.7, to the corresponding dimension-6 SMEFT Lagrangian, produces the Warsaw basis operators in Tab. A.1, where we distinguished the operators

$$\left(\mathcal{O}_{qq}^{(1)}\right)_{ij} = (\bar{q}_i \gamma_\mu q_i)(\bar{q}_j \gamma^\mu q_j), \quad \left(\mathcal{O}'_{qq}{}^{(1)}\right)_{ij} = (\bar{q}_i \gamma_\mu q_j)(\bar{q}_j \gamma^\mu q_i),$$

and

$$\left(\mathcal{O}_{qq}^{(3)}\right)_{ij} = (\bar{q}_i \tau^a \gamma_\mu q_i)(\bar{q}_j \tau^a \gamma^\mu q_j) \quad , \quad \left(\mathcal{O}'_{qq}{}^{(3)}\right)_{ij} = (\bar{q}_i \tau^a \gamma_\mu q_j)(\bar{q}_j \tau^a \gamma^\mu q_i),$$

where  $i, j$  are generation indices, and  $\tau^a$  are the Pauli matrices, i.e. the generators of the  $\text{SU}(2)_L$  group. In the literature, these operators are also respectively named *Direct* and *Exchange* [68].

Since we are interested in the top sector measurements, we restrict to a model with  $\text{U}(2)^3 = \text{U}(2)_q \times \text{U}(2)_u \times \text{U}(2)_d$  flavour symmetry, under which only the light quarks transform:

$$q \mapsto \text{U}_q q, \quad u \mapsto \text{U}_u u, \quad d \mapsto \text{U}_d d, \quad Q \mapsto Q, \quad t \mapsto t, \quad b \mapsto b \quad (\text{A.9})$$

4-fermion Operator	Warsaw basis	Top basis
$(\bar{L}L)(\bar{L}L)$	$\mathcal{O}_{qq}^{(1)}, \mathcal{O}'_{qq}{}^{(1)}, \mathcal{O}'_{qq}{}^{(3)}$	$\mathcal{O}_{Qq}^{(1,8)}$
$(\bar{R}R)(\bar{R}R)$	$\mathcal{O}_{uu}, \mathcal{O}'_{uu}, \mathcal{O}_{ud}^{(8)}$	$\mathcal{O}_{tu}^{(8)}, \mathcal{O}_{td}^{(8)}$
$(\bar{L}L)(\bar{R}R)$	$\mathcal{O}_{qu}^{(8)}, \mathcal{O}_{qd}^{(8)}$	$\mathcal{O}_{qt}^{(8)}, \mathcal{O}_{Qu}^{(8)}, \mathcal{O}_{Qd}^{(8)}$

**Table A.1.**  $\hat{Z}$  model Wilson operators generated by matching Eq. A.7 to the dimension-6 SMEFT, shown in the Warsaw and top bases.

where  $q$  is  $U(2)_q$  doublet containing the first two generations left-handed doublets,  $u$  is the  $U(2)_u$  doublet containing the first two up-type right-handed singlets,  $d$  is the  $U(2)_d$  doublet containing the first two down-type right-handed singlets,  $Q$  is the  $U(2)^3$  singlet which contains the heavy quark left-handed doublet, while  $t$  and  $b$  are the two  $U(2)^3$  singlets which contain the  $SU(2)_L$  singlets. Note that we neglect potential flavour mixing effects for simplicity.

We neglect purely light–light and heavy–heavy four-quark operators, which do not contribute to the observables considered in this analysis. The matching to the SMEFT then creates a point-like interaction between one heavy and one light quark  $SU(3)_c$  currents:

$$\mathcal{O}_{VV} = \sum_{i=1}^2 (\bar{Q}\gamma^\mu T^a Q + \bar{t}\gamma^\mu T^a t)(\bar{q}_i\gamma_\mu T^a q_i + \bar{u}_i\gamma_\mu T^a u_i + \bar{d}_i\gamma_\mu T^a d_i), \quad (\text{A.10})$$

Therefore, the restriction to the smaller set of Wilson operators [69, 70] shown in Tab. A.1 leads to the following definition of the SMEFT Lagrangian

$$\mathcal{L}_{\text{SMEFT}}^{\mathcal{G}} = \mathcal{L}_{\text{SM}} - \frac{g_s^2 \hat{Z}}{2m_W^2} \left[ \mathcal{O}_{Qq}^{(1,8)} + \mathcal{O}_{Qu}^{(8)} + \mathcal{O}_{Qd}^{(8)} + \mathcal{O}_{tu}^{(8)} + \mathcal{O}_{td}^{(8)} + \mathcal{O}_{qt}^{(8)} \right], \quad \hat{Z} = \frac{g_G^2 m_W^2}{g_s^2 M_G^2}, \quad (\text{A.11})$$

where  $\hat{Z}$  is the parameter which tunes the intensity of the new physics signature.

## B Presentation of the dataset

In this appendix, we present the real measurements used in the analysis of this project, mostly coming from the NNPDF [44] and SIMUnet [14] implementations. The HL-LHC projections have already been described in the main body of this paper in Tab. 3.1, 3.2 and 3.3.

Dataset	$N_{\text{dat}}$	$x$	$Q$ [GeV]	Ref.
NMC $d/p$	121	[0.002000, 0.675]	[0.400, 9.951]	[71]
NMC $p$	204	[0.004000, 0.479]	[0.894, 7.895]	[72]
SLAC $p$	33	[0.070000, 0.850]	[0.762, 5.400]	[73, 74]
SLAC $d$	34	[0.070000, 0.850]	[0.762, 5.393]	[73, 74]
BCDMS $p$	333	[0.070000, 0.750]	[2.739, 15.16]	[75]
BCDMS $d$	248	[0.070000, 0.750]	[2.958, 15.16]	[76]
CHORUS $\sigma_{CC}^{\nu}$	416	[0.020000, 0.650]	[0.513, 9.757]	[77]
CHORUS $\sigma_{CC}^{\bar{\nu}}$	416	[0.020000, 0.650]	[0.513, 9.757]	[77]
NuTeV $\sigma_c^{\nu}$	39	[0.021000, 0.326]	[1.062, 10.79]	[78]
NuTeV $\sigma_c^{\bar{\nu}}$	37	[0.015000, 0.207]	[0.875, 8.266]	[78]
HERA I+II incl. NC $e^-p$	159	[0.000800, 0.650]	[7.746, 223.6]	[79]
HERA I+II incl. NC $e^+p$ 460 GeV	204	[0.000046, 0.650]	[1.414, 28.28]	[79]
HERA I+II incl. NC $e^+p$ 575 GeV	254	[0.000028, 0.650]	[1.225, 28.28]	[79]
HERA I+II incl. NC $e^+p$ 820 GeV	70	[0.000001, 0.400]	[0.212, 173.2]	[79]
HERA I+II incl. NC $e^+p$ 920 GeV	377	[0.000005, 0.650]	[0.387, 173.2]	[79]
HERA I+II incl. CC $e^-p$	42	[0.008000, 0.650]	[17.32, 173.2]	[79]
HERA I+II incl. CC $e^+p$	39	[0.008000, 0.400]	[17.32, 173.2]	[79]
HERA comb. $\sigma_{cc}^{\text{red}}$	37	[0.000000, 0.050]	[1.581, 141.4]	[80]
HERA comb. $\sigma_{bb}^{\text{red}}$	26	[0.000000, 0.050]	[1.581, 141.4]	[80]
Total	3089			

**Table B.1.** Deep inelastic scattering datasets.  $F_2$  structure function, neutral- and charged-current cross-sections.

Dataset	$N_{\text{dat}}$	$p_T$ [GeV]	Ref.
ATLAS $W^+$ +jet 8 TeV	15	[12.5, 700]	[81]
ATLAS $W^-$ +jet 8 TeV	15	[12.5, 700]	[81]
Total	30		

**Table B.2.** Associated  $W^\pm$  vector bosons and jet production cross-section differential in the transverse momentum of the produced vector boson  $p_T^{W^\pm}$ .

Dataset	$N_{\text{dat}}$	$y$	$Q$ [GeV]	Ref.
DYE 866 $\sigma_{\text{DY}}^d/\sigma_{\text{DY}}^p$	15	[0.069, 1.530]	[4.6, 12.9]	[82]
DY E886 $\sigma_{\text{DY}}^p$	89	[0.000, 1.908]	[4.4, 15.8]	[83]
DY E605 $\sigma_{\text{DY}}^p$	85	[-0.20, 0.400]	[7.1, 16.9]	[84]
DYE 906 $\sigma_{\text{DY}}^d/\sigma_{\text{DY}}^p$	6	[0.107, 0.772]	[4.7, 6.36]	[85]
Total	195			

**Table B.3.** Fixed target Drell-Yan process datasets.

Dataset	$N_{\text{dat}}$	$\eta_{ll}$	$M_{ll}$ [GeV]	Ref.
ATLAS low-mass DY 2011 $d\sigma_{Z/\gamma^*}/dM_{ll}$	6	$[-2.10, 2.10]$	$[14.5, 56.0]$	[86]
ATLAS high-mass DY 7 TeV $d\sigma_{Z/\gamma^*}/dM_{ll}$	5	$[-2.10, 2.10]$	$[123, 1250]$	[87]
Total	11			

**Table B.4.** Neutral-current Drell-Yan cross-section differential in the invariant mass  $M_{ll}$  of the produced lepton-pair.

Dataset	$N_{\text{dat}}$	$p_T$ [GeV]	Ref.
ATLAS $Z p_T$ 8 TeV $(p_T^l, M_{ll})$	44	$[1, 550]$	[88]
Total	44		

**Table B.5.** Neutral-current Drell-Yan cross-section differential in the transverse momentum of the produced vector boson  $p_T^Z$ , i.e. the transverse momentum of the outgoing lepton pair  $p_T^l$ .

Dataset	$N_{\text{dat}}$	$y_{ll}$	$p_T^l$ [GeV]	Ref.
ATLAS $Z p_T$ 8 TeV $(p_T^l, y_{ll})$	48	$[0.2, 2.2]$	$[1, 550]$	[88]
CMS $Z p_T$ 8 TeV $(p_T^l, y_{ll})$	28	$[0.2, 1.8]$	$[10, 600]$	[89]
Total	76			

**Table B.6.** Neutral-current Drell-Yan cross-section double differential in the transverse momentum  $p_T^l$  and the rapidity  $y_{ll}$  of the produced lepton-pair.

Dataset	$N_{\text{dat}}$	$y$	$M$ [GeV]	Ref.
CDF $Z$ rapidity	28	[0.050, 2.800]	$M_Z$	[90]
D0 $Z$ rapidity	28	[0.050, 2.750]	$M_Z$	[91]
D0 $W \rightarrow \mu\nu$ asymmetry	9	[0.100, 1.880]	$M_W$	[92]
ATLAS $W, Z$ 7 TeV 2010	30	[0.105, 3.200]	$[M_W, M_Z]$	[93]
ATLAS $W, Z$ 7 TeV 2011 Central sel.	46	[0.100, 2.340]	[56, 133]	[94]
ATLAS $W, Z$ 7 TeV 2011 Forward sel.	15	[1.300, 3.400]	[91, 133]	[94]
ATLAS DY 2D 8 TeV high mass	48	[0.100, 2.300]	[133, 1000]	[95]
ATLAS DY 2D 8 TeV low mass	60	[0.100, 2.300]	[56, 175]	[96]
CMS $W$ asymmetry 840 pb	11	[0.100, 2.300]	$M_W$	[97]
CMS $W$ asymmetry 4.7 fb	11	[0.100, 2.250]	$M_W$	[98]
CMS Drell-Yan 2D 7 TeV 2011	110	[0.050, 2.350]	[25, 850]	[99]
CMS $W$ rapidity 8 TeV	22	[0.100, 2.250]	$M_W$	[100]
LHCb $Z$ 940 pb	9	[2.125, 4.125]	$M_Z$	[101]
LHCb $Z \rightarrow ee$ 2 fb	17	[2.062, 4.125]	$M_Z$	[102]
LHCb $W, Z \rightarrow \mu$ 7 TeV	29	[2.062, 4.250]	$[M_W, M_Z]$	[103]
LHCb $W, Z \rightarrow \mu$ 8 TeV	30	[2.062, 4.375]	$[M_W, M_Z]$	[104]
LHCb $Z \rightarrow \mu\mu$	16	[2.062, 4.375]	$M_Z$	[105]
LHCb $Z \rightarrow ee$	15	[2.062, 4.125]	$M_Z$	[102]
Total	534			

**Table B.7.** Drell-Yan datasets.

Dataset	$N_{\text{dat}}$	$\eta$	$p_T$ [GeV]	Ref.
ATLAS jets 8 TeV, R=0.6	171	[0.250, 2.750]	[77.50, 2246]	[106]
CMS jets 8 TeV	185	[0.250, 2.750]	[22.50, 2308]	[107]
Total	611			

**Table B.8.** Inclusive-jet cross-section double differential in the jet transverse momentum  $p_T$  and the jet absolute rapidity  $|y|$ .

Dataset	$N_{\text{dat}}$	$\eta$	$M_{\text{jj}}$ [GeV]	Ref.
ATLAS dijets 7 TeV, R=0.6	90	[0.25, 2.75]	[285.0, 4485]	[108]
CMS dijets 7 8TeV	54	[0.25, 2.25]	[246.5, 4381]	[109]
Total	144			

**Table B.9.** Dijets cross-section differential in the invariant mass of the jet-pair  $M_{\text{jj}}$  and the absolute rapidity separation of the jets  $|y^*|$ .

Dataset	$N_{\text{dat}}$	$\eta_\gamma$	$E_T^\gamma$ [GeV]	Ref.
ATLAS direct photon production 13 TeV	53	[0.125, 0.385]	[137.5, 1300]	[110]
Total	53			

**Table B.10.** Direct photon production cross-section differential in the photon transverse energy  $E_T^\gamma$ .

Dataset	$N_{\text{dat}}$	–	$M_{t\bar{t}}$ [GeV]	Ref.
ATLAS $t\bar{t}$ 8 TeV $m_{t\bar{t}}$ normalised	5	–	[350.0, 1850.0]	[111]
ATLAS $t\bar{t}$ 13 TeV $m_{t\bar{t}}$ normalised	8	–	[362.5, 1750.0]	[112]
CMS $t\bar{t}$ 8 TeV $m_{t\bar{t}}$ normalised	5	–	[340.0, 1300.0]	[113]
CMS $t\bar{t}$ 13 TeV $m_{t\bar{t}}$ normalised	14	–	[325.0, 2900.0]	[114]
ATLAS 8TeV $t\bar{t}$ asymmetry	1	–	$m_t$	[115]
ATLAS 13TeV $t\bar{t}$ asymmetry	5	–	[250.0, 1750.0]	[116]
CMS 8TeV $t\bar{t}$ asymmetry	3	–	[215.0, 5264.5]	[117]
CMS 13TeV $t\bar{t}$ asymmetry	3	–	[350.0, 1350.0]	[118]
ATLAS/CMS 8TeV $t\bar{t}$ asymmetry	6	–	[210.0, 975.0]	[119]
Total	50			

**Table B.11.**  $t\bar{t}$  cross-section differential in the invariant mass of the produced top-pair  $M_{t\bar{t}}$ , and  $t\bar{t}$  charge asymmetry inclusive at 8 TeV and differential in the top-pair invariant mass  $M_{t\bar{t}}$ .

Dataset	$N_{\text{dat}}$	–	$p_T$ [GeV]	Ref.
ATLAS 13TeV $t\bar{t}Z$	5	–	[20.0, 255]	[120]
CMS 13TeV $t\bar{t}Z$	3	–	[37.5, 375]	[121]
Total	8			

**Table B.12.** Associated  $t\bar{t}$  and  $Z$  boson production differential in the  $Z$  boson transverse momentum  $p_T^Z$  datasets.

Dataset	$N_{\text{dat}}$	$y_t$	$Q$ [GeV]	Ref.
ATLAS single top 7 TeV $y_t$ normalised	3	[0.100, 0.850]	$m_t$	[122]
ATLAS single antitop 7 TeV $y_{\bar{t}}$ normalised	3	[0.100, 0.850]	$m_t$	[122]
ATLAS single top 8 TeV $y_t$ normalised	3	[0.150, 1.000]	$m_t$	[123]
ATLAS single antitop 8 TeV $y_{\bar{t}}$ normalised	3	[0.150, 1.000]	$m_t$	[123]
CMS 13TeV single-top rapidity $y_t$	4	[0.100, 1.050]	$m_t$	[124]
Total	16			

**Table B.13.** Single top/antitop production distributions differential in the quark rapidity  $y_{t/\bar{t}}$ .

Dataset	$N_{\text{dat}}$	$y_{t\bar{t}}$	$Q$ [GeV]	Ref.
ATLAS $t\bar{t}$ 8 TeV $y_t$ normalised	4	[0.200, 2.050]	$m_t$	[125]
ATLAS $t\bar{t}$ 8 TeV $y_{t\bar{t}}$	4	[0.150, 1.900]	$m_t$	[125]
ATLAS $t\bar{t}$ 13 TeV ( $m_{t\bar{t}}, y_{t\bar{t}}$ )	10	[0.165, 2.025]	[350, 1985]	[126]
CMS $t\bar{t}$ 8 TeV $y_{t\bar{t}}$	9	[-1.820, 1.820]	$m_t$	[89]
CMS $t\bar{t}$ 13 TeV ( $m_{t\bar{t}}, y_{t\bar{t}}$ )	16	[0.175, 1.825]	[370, 1075]	[127]
Total	43			

**Table B.14.**  $t\bar{t}$  production cross-section differential in the rapidity of the top quark  $y_t$ , and the top-pair  $y_{t\bar{t}}$ .

Dataset	$N_{\text{dat}}$	–	$Q$ [GeV]	Ref.
ATLAS $W, Z$ incl. 13 TeV $\sigma^{fid}$	3	–	$[M_W, M_Z]$	[128]
ATLAS $\sigma_{tt}^{\text{tot}}$ 7 TeV	1	–	$m_t$	[129]
ATLAS $\sigma_{tt}^{\text{tot}}$ 8 TeV	1	–	$m_t$	[129]
ATLAS $\sigma_{tt}^{\text{tot}}$ (1+jets) 8 TeV	1	–	$m_t$	[130]
ATLAS $\sigma_{tt}^{\text{tot}}$ (dilepton) 13 TeV	1	–	$m_t$	[131]
ATLAS $\sigma_{tt}^{\text{tot}}$ (hadronic) 13 TeV	1	–	$m_t$	[126]
ATLAS $\sigma_{tt}^{\text{tot}}$ (1+jets) 13 TeV	1	–	$m_t$	[132]
CMS $\sigma_{tt}^{\text{tot}}$ 5 TeV	1	–	$m_t$	[133]
CMS $\sigma_{tt}^{\text{tot}}$ 7 TeV	1	–	$m_t$	[134]
CMS $\sigma_{tt}^{\text{tot}}$ 8 TeV	1	–	$m_t$	[134]
CMS $\sigma_{tt}^{\text{tot}}$ 13 TeV	1	–	$m_t$	[135]
CMS $\sigma_{tt}^{\text{tot}}$ (1+jets) 13 TeV	1	–	$m_t$	[114]
ATLAS $\sigma_{ttZ}^{\text{tot}}$ 8 TeV	1	–	$m_t$	[136]
ATLAS $\sigma_{ttW}^{\text{tot}}$ 8 TeV	1	–	$m_t$	[136]
ATLAS $\sigma_{ttZ}^{\text{tot}}$ 13 TeV	1	–	$m_t$	[137]
ATLAS $\sigma_{ttW}^{\text{tot}}$ 13 TeV	1	–	$m_t$	[137]
CMS $\sigma_{ttZ}^{\text{tot}}$ 8 TeV	1	–	$m_t$	[138]
CMS $\sigma_{ttW}^{\text{tot}}$ 8 TeV	1	–	$m_t$	[138]
CMS $\sigma_{ttZ}^{\text{tot}}$ 13 TeV	1	–	$m_t$	[139]
CMS $\sigma_{ttW}^{\text{tot}}$ 13 TeV	1	–	$m_t$	[139]
ATLAS $\sigma_t^{\text{tot}}$ 7 TeV	1	–	$m_t$	[122]
ATLAS $\sigma_{\bar{t}}^{\text{tot}}$ 7 TeV	1	–	$m_t$	[122]
ATLAS $\sigma_t^{\text{tot}}$ 8 TeV	1	–	$m_t$	[123]
ATLAS $\sigma_{\bar{t}}^{\text{tot}}$ 8 TeV	1	–	$m_t$	[123]
ATLAS $\sigma_t^{\text{tot}}$ in s-channel, 8 TeV	1	–	$m_t$	[140]
ATLAS $\sigma_t^{\text{tot}}$ 13 TeV	1	–	$m_t$	[141]
ATLAS $\sigma_{\bar{t}}^{\text{tot}}$ 13 TeV	1	–	$m_t$	[141]
ATLAS $\sigma_t^{\text{tot}}$ in s-channel, 13 TeV	1	–	$m_t$	[142]
CMS single top $\sigma_t + \sigma_{\bar{t}}$ 7 TeV	1	–	$m_t$	[143]
CMS $\sigma_t^{\text{tot}}$ 8 TeV	1	–	$m_t$	[144]
CMS $\sigma_{\bar{t}}^{\text{tot}}$ 8 TeV	1	–	$m_t$	[144]
CMS $\sigma_t^{\text{tot}}$ in s-channel, 8 TeV	1	–	$m_t$	[145]
CMS $\sigma_t^{\text{tot}}$ 13 TeV	1	–	$m_t$	[146]
CMS $\sigma_{\bar{t}}^{\text{tot}}$ 13 TeV	1	–	$m_t$	[146]
ATLAS $\sigma_{tW}^{\text{tot}}$ 8 TeV	1	–	$m_t$	[147]
ATLAS $\sigma_{tW}^{\text{tot}}$ (single lepton) 8 TeV	1	–	$m_t$	[148]
ATLAS $\sigma_{tW}^{\text{tot}}$ 13 TeV	1	–	$m_t$	[149]
CMS $\sigma_{tW}^{\text{tot}}$ 8 TeV	1	–	$m_t$	[150]
CMS $\sigma_{tW}^{\text{tot}}$ 13 TeV	1	–	$m_t$	[151]
CMS $\sigma_{tW}^{\text{tot}}$ (single lepton) 13 TeV	1	–	$m_t$	[152]
Total	42			

**Table B.15.** Inclusive  $t\bar{t}$  production cross-section datasets.

## C Evaluation of fit qualities

In this appendix, we present the quality of the different fits performed in this study. We show their  $\Delta\chi^2$  dataset-per-dataset as well as the global  $\Delta\chi^2$  (taking into account the

correlations between the datasets) with respect to a baseline SM-like fit, specified in each case.

In Tab. C.1 we display the  $\Delta\chi^2$  of the fits performed on the Drell-Yan sector in the presence of both a  $W'$  ( $\hat{W} = 8 \times 10^{-5}$ ) and a  $Z'$  ( $\hat{Y} = 1.5 \times 10^{-4}$ ) displayed in Fig. 3.5 for the SMEFT and in Fig. 3.6 for the PDFs. We use the separate fit using the "True PDF" as the baseline and compute with respect to it the  $\Delta\chi^2$  of the conservative fit, the simultaneous fit and the BSM-biased fit dataset-per-dataset.

In Tab. C.2 we show the same comparison for the fits on the  $t\bar{t}$  sector in the presence of a heavy gluon with  $\hat{Z} = 4 \times 10^{-4}$ . The fit results were displayed in Fig. 3.9 for the SMEFT and on Fig. 3.8 for the PDF marginal distributions.

Finally, in Tab. C.3 we compare the separate PDF and SMEFT fits performed with various energy cuts on the PDF dataset presented in Fig. 4.1. Here, the SMEFT fit obtained using PDFs fitted to the full set of SM data is taken as the reference, and the  $\Delta\chi^2$  values of the other fits are computed relative to this baseline.

Dataset	$n_{\text{dat}}$	$\Delta\chi^2$		
		SMEFT Fit (BSM biased)	Conservative Fit	Simultaneous Fit
NMC $d/p$	121	+0.912	+0.020	-0.025
NMC $p$	204	+0.178	-0.021	-0.025
SLAC $p$	33	+0.012	-0.001	-0.004
SLAC $d$	34	+0.040	-0.004	-0.006
BCDMS $p$	333	+0.075	-0.042	-0.085
BCDMS $d$	248	+0.325	-0.011	-0.028
CHORUS $\sigma_{CC\nu}$	416	+0.307	-0.014	-0.035
CHORUS $\sigma_{CC}^{\bar{\nu}}$	416	+1.041	-0.005	-0.025
NuTeV $\sigma_c^{\nu}$	39	+0.250	-0.012	-0.013
NuTeV $\sigma_c^{\bar{\nu}}$	37	+3.029	+0.030	+0.016
HERA I+II inclusive NC $e^-p$	159	+0.131	-0.006	-0.018
HERA I+II inclusive NC $e^+p$ 460 GeV	204	+0.021	-0.007	-0.007
HERA I+II inclusive NC $e^+p$ 575 GeV	254	+0.031	-0.005	-0.005
HERA I+II inclusive NC $e^+p$ 820 GeV	70	+0.080	-0.003	-0.003
HERA I+II inclusive NC $e^+p$ 920 GeV	377	+0.584	-0.052	-0.055
HERA I+II inclusive CC $e^-p$	42	+0.030	-0.001	-0.002
HERA I+II inclusive CC $e^+p$	39	+0.344	-0.003	-0.010
HERA comb. $\sigma_{c\bar{c}}^{\text{red}}$	37	+0.239	-0.015	-0.013
HERA comb. $\sigma_{b\bar{b}}^{\text{red}}$	26	+0.001	-0.000	-0.000
CDF $Z$ rapidity (new)	28	+0.224	-0.014	-0.020
D0 $Z$ rapidity	28	+0.062	-0.003	-0.003
D0 $W \rightarrow \mu\nu$ asymmetry	9	+0.307	-0.069	-0.070
ATLAS $W, Z$ inclusive 13 TeV	3	+0.002	-0.009	-0.007
ATLAS $W^+$ +jet 8 TeV	15	+0.032	+0.000	+0.000
ATLAS $W^-$ +jet 8 TeV	15	+0.074	-0.000	-0.001
ATLAS direct photon production 13 TeV	53	+0.118	-0.002	-0.002
ATLAS $W, Z$ 7 TeV 2011 Central selection	46	+0.330	-0.002	-0.014
ATLAS $W, Z$ 7 TeV 2010	30	+0.035	+0.000	+0.000
ATLAS $W, Z$ 7 TeV 2011 Forward selection	15	+0.015	-0.001	-0.002
ATLAS $Z$ $p_T$ 8 TeV ( $p_T^l, M_{ll}$ )	44	+0.061	-0.000	-0.001
ATLAS $Z$ $p_T$ 8 TeV ( $p_T^l, y_{ll}$ )	48	+0.195	-0.017	-0.012
CMSZDIFF12	28	+0.030	-0.003	-0.002
CMS $W$ asymmetry 840 pb	11	+0.232	+0.008	+0.004
CMS $W$ asymmetry 4.7 fb	11	+0.048	-0.017	-0.013
CMS $W$ rapidity 8 TeV	22	+0.086	+0.025	-0.011
LHCb $Z$ 940 pb	9	+0.008	-0.001	-0.001
LHCb $Z \rightarrow ee$ 2 fb	17	+0.026	-0.004	-0.004
LHCb $W, Z \rightarrow \mu$ 7 TeV	29	+1.232	-0.039	-0.049

*Continued on next page*

LHCb $W, Z \rightarrow \mu$ 8 TeV	30	+1.490	-0.057	-0.053
LHCb $Z \rightarrow \mu\mu$	16	+0.004	-0.000	-0.001
LHCb $Z \rightarrow ee$	15	+0.001	-0.000	-0.000
DYE 866 $\sigma_{DY}^d/\sigma_{DY}^p$	15	+0.324	-0.009	+0.005
DY E886 $\sigma_{DY}^p$	89	+8.849	-0.025	-0.064
DY E605 $\sigma_{DY}^p$	85	+0.283	+0.004	-0.006
DYE 906 $\sigma_{DY}^d/\sigma_{DY}^p$	6	+0.417	-0.006	-0.029
ATLAS DY 2D 8 TeV low mass	60	+0.058	-0.006	-0.014
HL-LHC Forward Drell-Yan 14 TeV - $W^-$ -	8	+0.376	+0.008	-0.013
HL-LHC Forward Drell-Yan 14 TeV - $W^+$	8	+0.522	+0.002	-0.015
ATLAS DY 2D 8 TeV high mass	48	+0.947	-0.009	-0.031
ATLAS low-mass DY 2011	6	+0.001	+0.000	-0.000
CMS DY 2D 7 TeV	110	+0.089	+0.014	-0.001
CMS DY 1D 8 TeV	41	+0.566	+0.014	-0.012
ATLAS HM DY 7 TeV	5	+0.020	+0.002	-0.000
CMS HM DY 13 TeV - combined channel	43	+0.057	+0.003	-0.002
HL-LHC HM DY 14 TeV - neutral current - electron channel	12	+1.852	+0.104	+0.035
HL-LHC HM DY 14 TeV - neutral current - muon channel	12	+1.856	+0.104	+0.035
HL-LHC HM DY 14 TeV - charged current - electron channel	16	+3.104	+0.083	+0.036
GLOBAL	4363	+31.964	-0.117	-0.728

**Table C.1.** The total dataset  $\Delta\chi^2$  for datasets entering the SMEFT and PDF fits, presented respectively in Fig. 3.5 and in Fig. 3.6 for the DY sector analysis. For each dataset, we indicate the number of data points  $n_{\text{dat}}$  and the corresponding  $\Delta\chi^2$  with respect to the fit using the true PDF, chosen as a reference.

Dataset	$n_{\text{dat}}$	$\Delta\chi^2$		
		SMEFT Fit (BSM biased)	Conservative Fit	Simultaneous Fit
ATLAS $\sigma_{t\bar{t}}^{\text{tot}}$ 7 TeV	1	+0.018	+0.000	+0.000
ATLAS $\sigma_{t\bar{t}}^{\text{tot}}$ 8 TeV	1	+0.010	+0.000	+0.000
ATLAS $t\bar{t}$ 8 TeV $y_{t\bar{t}}$ normalised	4	+0.559	+0.017	-0.006
ATLAS $t\bar{t}$ 8 TeV $m_{t\bar{t}}$ normalised	5	+0.014	+0.000	+0.000
ATLAS $\sigma_{t\bar{t}}^{\text{tot}}$ (1+jets) 8 TeV	1	+0.005	+0.000	+0.000
ATLAS $t\bar{t}$ 13 TeV $m_{t\bar{t}}$ normalised	8	+0.015	+0.000	+0.000
ATLAS $t\bar{t}$ 13 TeV ( $m_{t\bar{t}}, y_{t\bar{t}}$ )	10	+0.550	+0.009	-0.001
ATLAS $\sigma_{t\bar{t}}^{\text{tot}}$ (1+jets) 13 TeV	1	+0.000	+0.000	+0.000
ATLAS $\sigma_{t\bar{t}}^{\text{tot}}$ (dilepton) 13 TeV	1	-0.000	+0.000	+0.000
ATLAS $\sigma_{t\bar{t}}^{\text{tot}}$ (hadronic) 13 TeV	1	+0.000	+0.000	+0.000
CMS $\sigma_{t\bar{t}}^{\text{tot}}$ 5 TeV	1	+0.006	+0.000	+0.000
CMS $\sigma_{t\bar{t}}^{\text{tot}}$ 7 TeV	1	+0.025	+0.000	+0.000
CMS $\sigma_{t\bar{t}}^{\text{tot}}$ 8 TeV	1	+0.014	+0.000	+0.000
CMS $\sigma_{t\bar{t}}^{\text{tot}}$ 13 TeV	1	+0.000	+0.000	+0.000
CMS $t\bar{t}$ 8 TeV $y_{t\bar{t}}$	9	+1.239	+0.017	-0.005
CMS $t\bar{t}$ 13 TeV ( $m_{t\bar{t}}, y_{t\bar{t}}$ )	16	+0.623	+0.010	-0.002
CMS $t\bar{t}$ 8 TeV $m_{t\bar{t}}$ normalised	5	+0.014	-0.000	-0.000
CMS $t\bar{t}$ 13 TeV $m_{t\bar{t}}$ normalised	14	+0.156	+0.000	-0.000
CMS $\sigma_{t\bar{t}}^{\text{tot}}$ (1+jets) 13 TeV	1	+0.000	+0.000	+0.000
HL-LHC high-mass $t\bar{t}$ production	18	+1.182	+0.009	-0.004
GLOBAL	4363	+5.131	+0.107	+0.034

**Table C.2.** The total dataset  $\chi^2$  for datasets entering the SMEFT and PDF fits in the top sector analysis, presented respectively in Fig. 3.9 and in Fig. 3.8. For each dataset, we indicate the number of data points  $n_{\text{dat}}$  and the corresponding  $\Delta\chi^2$  with respect to the fit using the true PDF, chosen as a reference.

Dataset	$n_{\text{dat}}$	$\Delta\chi^2$			
		Full Data Contaminated	1500GeV Cut Contaminated	1000GeV Cut Contaminated	500GeV Cut Contaminated
ATLAS $W, Z$ inclusive 13 TeV	3	-0.003	-0.010	-0.007	-0.013
ATLAS $W^+$ +jet 8 TeV	15	+0.034	+0.023	+0.013	-0.000
ATLAS $W^-$ +jet 8 TeV	15	+0.051	+0.018	+0.006	+0.000
ATLAS direct photon production 13 TeV	53	+0.035	+0.021	+0.007	-0.002
ATLAS $W, Z$ 7 TeV 2011 Central selection	46	+0.216	+0.030	-0.021	-0.047
ATLAS $W, Z$ 7 TeV 2010	30	+0.023	+0.012	+0.003	-0.004
ATLAS $W, Z$ 7 TeV 2011 Forward selection	15	+0.011	-0.003	-0.004	-0.002
ATLAS $Z$ $p_T$ 8 TeV ( $p_T^l, M_{ll}$ )	44	+0.018	+0.013	+0.006	-0.001
ATLAS $Z$ $p_T$ 8 TeV ( $p_T^l, y_{ll}$ )	48	+0.206	+0.047	+0.014	-0.023
CMS $Z$ $p_T$ 8 TeV ( $p_T^l, y_{ll}$ )	28	+0.028	+0.018	+0.007	-0.004
CMS $W$ asymmetry 840 pb	11	+0.142	+0.229	+0.187	+0.002
CMS $W$ asymmetry 4.7 fb	11	-0.027	-0.008	+0.002	-0.024
CMS $W$ rapidity 8 TeV	22	+0.160	+0.081	+0.143	-0.023
LHCb $Z$ 940 pb	9	+0.007	-0.001	-0.001	-0.002
LHCb $Z \rightarrow ee$ 2 fb	17	+0.021	-0.000	-0.002	-0.006
LHCb $W, Z \rightarrow \mu$ 7 TeV	29	+0.863	+0.235	+0.142	-0.066
LHCb $W, Z \rightarrow \mu$ 8 TeV	30	+1.003	+0.291	+0.160	-0.085
LHCb $Z \rightarrow \mu\mu$	16	+0.005	+0.002	-0.000	-0.002
LHCb $Z \rightarrow ee$	15	+0.003	+0.001	+0.000	-0.001
DYE 866 $\sigma_{\text{DY}}^d / \sigma_{\text{DY}}^p$	15	+1.183	+0.574	+0.332	-0.011
DY E886 $\sigma_{\text{DY}}^p$	89	+3.511	+0.855	+0.224	-0.036
DY E605 $\sigma_{\text{DY}}^p$	85	+0.147	+0.072	+0.042	-0.002
DYE 906 $\sigma_{\text{DY}}^d / \sigma_{\text{DY}}^p$	6	+0.490	+0.060	+0.032	-0.019
ATLAS DY 2D 8 TeV low mass	60	+0.039	-0.012	-0.013	-0.012
HL-LHC Forward Drell-Yan 14 TeV (CC) $\mu+$	8	+0.265	+0.070	+0.049	-0.034
HL-LHC Forward Drell-Yan 14 TeV (CC) $\mu$	8	+0.419	+0.019	-0.035	-0.008
HL-LHC Forward Drell-Yan 14 TeV (NC)	18	+0.161	+0.013	-0.011	-0.036
ATLAS DY 2D 8 TeV high mass	48	+0.362	+0.331	+0.197	-0.044
ATLAS low-mass DY 2011	6	-0.000	-0.001	-0.001	+0.000
CMS Drell-Yan 2D 7 TeV 2011	110	+0.031	+0.019	+0.015	+0.007
CMS DY 1D 8 TeV	41	+0.359	+0.220	+0.155	-0.014
ATLAS high-mass DY 7 TeV $d\sigma_{Z/\gamma^*} / dM_{ll}$	5	+0.007	+0.007	+0.006	+0.000
CMS HM DY 13 TeV - combined channel	43	+0.053	+0.025	+0.019	-0.003
HL-LHC High-mass Drell-Yan (NC) (electron)	12	+0.258	+0.826	+0.680	+0.056
HL-LHC High-mass Drell-Yan (NC) (muon)	12	+0.252	+0.812	+0.668	+0.056
HL-LHC High-mass Drell-Yan (CC) (electron)	16	+3.158	+6.101	+4.301	+0.012
GLOBAL	4363	+20.857	+13.241	+8.215	-1.154

**Table C.3.** The total dataset  $\chi^2$  for datasets entering the SMEFT and PDF fits for the energy cut-off analysis, presented in Fig. 4.1. Only the DY sector has been presented. For each dataset, we indicate the number of data points  $n_{\text{dat}}$  and the corresponding  $\Delta\chi^2$  with respect to the fit using the true PDF, chosen as a reference.

## References

- [1] D. E. Morrissey, T. Plehn, and T. M. P. Tait, *Physics searches at the LHC*, Phys. Rept. **515** (2012) 1–113, [[arXiv:0912.3259](#)].
- [2] **GAMBIT** Collaboration, P. Athron et al., *Global fits and the search for new physics: past, present and future*, [arXiv:2512.14109](#).
- [3] S. Carrazza, C. Degrande, S. Iranipour, J. Rojo, and M. Ubiali, *Can New Physics hide inside the proton?*, Phys. Rev. Lett. **123** (2019), no. 13 132001, [[arXiv:1905.05215](#)].
- [4] A. Greljo, S. Iranipour, Z. Kassabov, M. Madigan, J. Moore, J. Rojo, M. Ubiali, and C. Voisey, *Parton distributions in the SMEFT from high-energy Drell-Yan tails*, JHEP **07** (2021) 122, [[arXiv:2104.02723](#)].

- [5] CMS Collaboration, A. Tumasyan et al., *Measurement and QCD analysis of double-differential inclusive jet cross sections in proton-proton collisions at  $\sqrt{s} = 13$  TeV*, JHEP **02** (2022) 142, [[arXiv:2111.10431](#)]. [Addendum: JHEP 12, 035 (2022)].
- [6] S. Iranipour and M. Ubiali, *A new generation of simultaneous fits to LHC data using deep learning*, JHEP **05** (2022) 032, [[arXiv:2201.07240](#)].
- [7] J. Gao, M. Gao, T. J. Hobbs, D. Liu, and X. Shen, *Simultaneous CTEQ-TEA extraction of PDFs and SMEFT parameters from jet and  $t\bar{t}$  data*, JHEP **05** (2023) 003, [[arXiv:2211.01094](#)].
- [8] R. D. Ball, A. Candido, S. Forte, F. Hekhorn, E. R. Nocera, J. Rojo, and C. Schwan, *Parton distributions and new physics searches: the Drell–Yan forward–backward asymmetry as a case study*, Eur. Phys. J. C **82** (2022), no. 12 1160, [[arXiv:2209.08115](#)].
- [9] M. McCullough, J. Moore, and M. Ubiali, *The dark side of the proton*, JHEP **08** (2022) 019, [[arXiv:2203.12628](#)].
- [10] Z. Kassabov, M. Madigan, L. Mantani, J. Moore, M. Morales Alvarado, J. Rojo, and M. Ubiali, *The top quark legacy of the LHC Run II for PDF and SMEFT analyses*, JHEP **05** (2023) 205, [[arXiv:2303.06159](#)].
- [11] E. Hammou, Z. Kassabov, M. Madigan, M. L. Mangano, L. Mantani, J. Moore, M. M. Alvarado, and M. Ubiali, *Hide and seek: how PDFs can conceal new physics*, JHEP **11** (2023) 090, [[arXiv:2307.10370](#)].
- [12] E. Hammou and M. Ubiali, *Unravelling new physics signals at the HL-LHC with EIC and FPF constraints*, Phys. Rev. D **111** (2025), no. 9 095028, [[arXiv:2410.00963](#)].
- [13] X. Shen, S. Amoroso, J. Gao, K. Lipka, and O. Zenaiev, *A framework for simultaneous fit of QCD and BSM parameters with  $x$ Fitter*, Eur. Phys. J. C **84** (2024), no. 11 1235, [[arXiv:2407.16061](#)].
- [14] PBSP Collaboration, M. N. Costantini, E. Hammou, Z. Kassabov, M. Madigan, L. Mantani, M. Morales Alvarado, J. M. Moore, and M. Ubiali, *SIMUnet: an open-source tool for simultaneous global fits of EFT Wilson coefficients and PDFs*, Eur. Phys. J. C **84** (2024), no. 8 805, [[arXiv:2402.03308](#)].
- [15] M. Farina, C. Mondino, D. Pappadopulo, and J. T. Ruderman, *New physics from high energy tops*, [arXiv:1811.04084](#).
- [16] A. Greljo, E. Hammou, F. Merlotti, A. Smolkovic, and M. Ubiali, “Jets anomalies and interplay with the large- $x$  gluon.” in preparation.
- [17] R. Gómez-Ambrosio, L. Mantani, E. R. Nocera, and M. Ubiali, “Anomalous gluon interaction: a critical re-appraisal.” in preparation.
- [18] E. C. Aschenauer, S. Fazio, J. H. Lee, H. Mantysaari, B. S. Page, B. Schenke, T. Ullrich, R. Venugopalan, and P. Zurita, *The electron–ion collider: assessing the energy dependence of key measurements*, Rept. Prog. Phys. **82** (2019), no. 2 024301, [[arXiv:1708.01527](#)].
- [19] FASER Collaboration, H. Abreu et al., *The FASER detector*, JINST **19** (2024), no. 05 P05066, [[arXiv:2207.11427](#)].
- [20] L. Del Debbio, T. Giani, J. Karpie, K. Orginos, A. Radyushkin, and S. Zafeiropoulos, *Neural-network analysis of Parton Distribution Functions from Ioffe-time pseudodistributions*, JHEP **02** (2021) 138, [[arXiv:2010.03996](#)].

- [21] M. N. Costantini, L. Mantani, J. M. Moore, V. S. Sanchez, and M. Ubiali, *Colibri: A new tool for fast-flying PDF fits*, *Eur. Phys. J. C* ”86” (”2026”), no. ”1” ”22”, [[arXiv:2510.03391](#)].
- [22] M. N. Costantini, L. Mantani, J. M. Moore, and M. Ubiali, *A linear PDF model for Bayesian inference*, [arXiv:2507.16913](#).
- [23] T. Giani, G. Magni, and J. Rojo, *SMEFiT: a flexible toolbox for global interpretations of particle physics data with effective field theories*, [arXiv:2302.06660](#).
- [24] J. ter Hoeve, G. Magni, J. Rojo, A. N. Rossia, and E. Vryonidou, *The automation of SMEFT-assisted constraints on UV-complete models*, *JHEP* **01** (2024) 179, [[arXiv:2309.04523](#)].
- [25] E. Celada, T. Giani, J. ter Hoeve, L. Mantani, J. Rojo, A. N. Rossia, M. O. A. Thomas, and E. Vryonidou, *Mapping the SMEFT at high-energy colliders: from LEP and the (HL-)LHC to the FCC-ee*, *JHEP* **09** (2024) 091, [[arXiv:2404.12809](#)].
- [26] J. ter Hoeve, L. Mantani, J. Rojo, A. N. Rossia, and E. Vryonidou, *Connecting scales: RGE effects in the SMEFT at the LHC and future colliders*, *JHEP* **06** (2025) 125, [[arXiv:2502.20453](#)].
- [27] J. ter Hoeve, L. Mantani, J. Rojo, A. N. Rossia, and E. Vryonidou, *Higgs trilinear coupling in the standard model effective field theory at the high luminosity LHC and the FCC-ee*, *Phys. Rev. D* **112** (2025), no. 1 013008, [[arXiv:2504.05974](#)].
- [28] **SMEFiT** Collaboration, J. J. Ethier, G. Magni, F. Maltoni, L. Mantani, E. R. Nocera, J. Rojo, E. Slade, E. Vryonidou, and C. Zhang, *Combined SMEFT interpretation of Higgs, diboson, and top quark data from the LHC*, *JHEP* **11** (2021) 089, [[arXiv:2105.00006](#)].
- [29] X.-M. Shen, J. Gao, M. Gao, T. J. Hobbs, and D. Liu, *Determining SMEFT and PDF parameters simultaneously based on the CTEQ-TEA framework*, *PoS EPS-HEP2023* (2024) 291.
- [30] **NNPDF** Collaboration, R. D. Ball et al., *Parton distributions for the LHC Run II*, *JHEP* **04** (2015) 040, [[arXiv:1410.8849](#)].
- [31] L. Del Debbio, T. Giani, and M. Wilson, *Bayesian approach to inverse problems: an application to NNPDF closure testing*, *Eur. Phys. J. C* **82** (2022), no. 4 330, [[arXiv:2111.05787](#)].
- [32] A. Barontini, M. N. Costantini, G. De Crescenzo, S. Forte, and M. Ubiali, *Evaluating the faithfulness of PDF uncertainties in the presence of inconsistent data*, [arXiv:2503.17447](#).
- [33] **NNPDF** Collaboration, R. D. Ball et al., *The path to  $N^3LO$  parton distributions*, *Eur. Phys. J. C* **84** (2024), no. 7 659, [[arXiv:2402.18635](#)].
- [34] **NNPDF** Collaboration, R. D. Ball et al., *Determination of the theory uncertainties from missing higher orders on NNLO parton distributions with percent accuracy*, *Eur. Phys. J. C* **84** (2024), no. 5 517, [[arXiv:2401.10319](#)].
- [35] **NNPDF** Collaboration, R. D. Ball et al., *The path to proton structure at 1% accuracy*, *Eur. Phys. J. C* **82** (2022), no. 5 428, [[arXiv:2109.02653](#)].
- [36] R. Frederix, S. Frixione, V. Hirschi, D. Pagani, H. S. Shao, and M. Zaro, *The automation of next-to-leading order electroweak calculations*, *JHEP* **07** (2018) 185, [[arXiv:1804.10017](#)].
- [37] A. Greljo, S. Iranipour, Z. Kassabov, M. Madigan, J. Moore, J. Rojo, M. Ubiali, and

- C. Voisey, *Parton distributions in the SMEFT from high-energy Drell-Yan tails*, JHEP **07** (2021) 122, [[arXiv:2104.02723](#)].
- [38] A. Barontini, A. Candido, J. M. Cruz-Martinez, F. Hekhorn, and C. Schwan, *Pipeline: Industrialization of high-energy theory predictions*, Comput. Phys. Commun. **297** (2024) 109061, [[arXiv:2302.12124](#)].
- [39] NNLOJET Collaboration, A. Huss et al., *NNLOJET: a parton-level event generator for jet cross sections at NNLO QCD accuracy*, [arXiv:2503.22804](#).
- [40] LHCb Collaboration, R. Aaij et al., *Measurement of forward  $W$  and  $Z$  boson production in  $pp$  collisions at  $\sqrt{s} = 8$  TeV*, JHEP **01** (2016) 155, [[arXiv:1511.08039](#)].
- [41] G. Durieux, A. G. Camacho, L. Mantani, V. Miralles, M. M. López, M. Llácer Moreno, R. Poncelet, E. Vryonidou, and M. Vos, *Snowmass White Paper: prospects for the measurement of top-quark couplings*, in Snowmass 2021, 5, 2022. [arXiv:2205.02140](#).
- [42] M. Czakon, D. Heymes, and A. Mitov, *Dynamical scales for multi-TeV top-pair production at the LHC*, [arXiv:1606.03350](#).
- [43] M. Czakon, Z. Kassabov, A. Mitov, R. Poncelet, and A. Popescu, *HighTEA: high energy theory event analyser*, J. Phys. G **51** (2024), no. 11 115002, [[arXiv:2304.05993](#)].
- [44] NNPDF Collaboration, R. D. Ball et al., *The path to proton structure at 1% accuracy*, Eur. Phys. J. C **82** (2022), no. 5 428, [[arXiv:2109.02653](#)].
- [45] ATLAS Collaboration, G. Aad et al., *Measurement of the high-mass Drell-Yan differential cross-section in  $pp$  collisions at  $\sqrt{s}=7$  TeV with the ATLAS detector*, Phys. Lett. B **725** (2013) 223–242, [[arXiv:1305.4192](#)].
- [46] ATLAS Collaboration, G. Aad et al., *Measurement of the double-differential high-mass Drell-Yan cross section in  $pp$  collisions at  $\sqrt{s} = 8$  TeV with the ATLAS detector*, JHEP **08** (2016) 009, [[arXiv:1606.01736](#)].
- [47] CMS Collaboration, S. Chatrchyan et al., *Measurement of the Differential and Double-Differential Drell-Yan Cross Sections in Proton-Proton Collisions at  $\sqrt{s} = 7$  TeV*, JHEP **12** (2013) 030, [[arXiv:1310.7291](#)].
- [48] CMS Collaboration, V. Khachatryan et al., *Measurements of differential and double-differential Drell-Yan cross sections in proton-proton collisions at 8 TeV*, Eur. Phys. J. C **75** (2015), no. 4 147, [[arXiv:1412.1115](#)].
- [49] CMS Collaboration, A. M. Sirunyan et al., *Measurement of the differential Drell-Yan cross section in proton-proton collisions at  $\sqrt{s} = 13$  TeV*, JHEP **12** (2019) 059, [[arXiv:1812.10529](#)].
- [50] M. Farina, G. Panico, D. Pappadopulo, J. T. Ruderman, R. Torre, and A. Wulzer, *Energy helps accuracy: electroweak precision tests at hadron colliders*, Phys. Lett. **B772** (2017) 210–215, [[arXiv:1609.08157](#)].
- [51] M. Beneke, P. Falgari, S. Klein, J. Piclum, C. Schwinn, et al., *Inclusive Top-Pair Production Phenomenology with TOPIXS*, JHEP **1207** (2012) 194, [[arXiv:1206.2454](#)].
- [52] M. Czakon, M. L. Mangano, A. Mitov, and J. Rojo, *Constraints on the gluon PDF from top quark pair production at hadron colliders*, JHEP **1307** (2013) 167, [[arXiv:1303.7215](#)].
- [53] E. R. Nocera and M. Ubiali, *Constraining the gluon PDF at large  $x$  with LHC data*, PoS **DIS2017** (2018) 008, [[arXiv:1709.09690](#)].

- [54] R. Barbieri, A. Pomarol, R. Rattazzi, and A. Strumia, *Electroweak symmetry breaking after LEP1 and LEP2*, [hep-ph/0405040](#).
- [55] R. S. Chivukula, A. G. Cohen, and E. H. Simmons, *New strong interactions at the Tevatron?*, Phys. Lett. B **380** (1996) 92–98, [[hep-ph/9603311](#)].
- [56] E. H. Simmons, *Coloron phenomenology*, Phys. Rev. D **55** (1997) 1678–1683, [[hep-ph/9608269](#)].
- [57] M. L. Mangano and J. Rojo, *Cross Section Ratios between different CM energies at the LHC: opportunities for precision measurements and BSM sensitivity*, JHEP **1208** (2012) 010, [[arXiv:1206.3557](#)].
- [58] R. Abdul Khalek et al., *Snowmass 2021 White Paper: Electron Ion Collider for High Energy Physics*, [arXiv:2203.13199](#).
- [59] **FPF** Collaboration, L. A. Anchordoqui et al., *Letter of Intent: The Forward Physics Facility*, [arXiv:2510.26260](#).
- [60] F. Ahmadova et al., *The Large Hadron electron Collider as a bridge project for CERN*, [arXiv:2503.17727](#).
- [61] **ATLAS** Collaboration, M. Aaboud et al., *Measurement of inclusive jet and dijet cross-sections in proton-proton collisions at  $\sqrt{s} = 13$  TeV with the ATLAS detector*, JHEP **05** (2018) 195, [[arXiv:1711.02692](#)].
- [62] D. Britzger et al., *NNLO interpolation grids for jet production at the LHC*, Eur. Phys. J. C **82** (2022), no. 10 930, [[arXiv:2207.13735](#)].
- [63] A. Chiefa, M. N. Costantini, J. Cruz-Martinez, E. R. Nocera, T. R. Rabemananjara, J. Rojo, T. Sharma, R. Stegeman, and M. Ubiali, *Parton distributions confront LHC Run II data: a quantitative appraisal*, JHEP **07** (2025) 067, [[arXiv:2501.10359](#)].
- [64] S. Carrazza, E. R. Nocera, C. Schwan, and M. Zaro, *PineAPPL: combining EW and QCD corrections for fast evaluation of LHC processes*, JHEP **12** (2020) 108, [[arXiv:2008.12789](#)].
- [65] M. Hirsch, L. Mantani, and V. Sanz, *Data-Driven Discovery Strategy for Standard Model Effective Field Theory Searches*, Phys. Rev. Lett. **135** (2025), no. 24 241801, [[arXiv:2507.11109](#)].
- [66] M. Ubiali, *Modern Machine Learning and Particle Physics Phenomenology at the LHC*, in 2nd European AI for Fundamental Physics Conference, 2, 2026. [arXiv:2602.03728](#).
- [67] J. D. Wells and Z. Zhang, *Effective theories of universal theories*, JHEP **01** (2016) 123, [[arXiv:1510.08462](#)].
- [68] A. Greljo and A. Palavrić, *Leading directions in the SMEFT*, . [arXiv:2305.08898](#) [hep-ex, physics:hep-ph].
- [69] J. Ellis, M. Madigan, K. Mimasu, V. Sanz, and T. You, *Top, Higgs, Diboson and Electroweak Fit to the Standard Model Effective Field Theory*, JHEP **04** (2021) 279, [[arXiv:2012.02779](#)].
- [70] D. Barducci et al., *Interpreting top-quark LHC measurements in the standard-model effective field theory*, [arXiv:1802.07237](#).
- [71] **New Muon** Collaboration, M. Arneodo et al., *Accurate measurement of  $F_2^d/F_2^p$  and  $R_d - R_p$* , Nucl. Phys. **B487** (1997) 3–26, [[hep-ex/9611022](#)].

- [72] **New Muon** Collaboration, M. Arneodo et al., *Measurement of the proton and deuteron structure functions,  $F_2^p$  and  $F_2^d$ , and of the ratio  $\sigma_L/\sigma_T$* , Nucl. Phys. **B483** (1997) 3–43, [[hep-ph/9610231](#)].
- [73] L. W. Whitlow, S. Rock, A. Bodek, E. M. Riordan, and S. Dasu, *A Precise extraction of  $R = \sigma_{L-T} / \sigma_{L+T}$  from a global analysis of the SLAC deep inelastic  $e p$  and  $e d$  scattering cross-sections*, Phys. Lett. B **250** (1990) 193–198.
- [74] L. W. Whitlow, E. M. Riordan, S. Dasu, S. Rock, and A. Bodek, *Precise measurements of the proton and deuteron structure functions from a global analysis of the SLAC deep inelastic electron scattering cross-sections*, Phys. Lett. **B282** (1992) 475–482.
- [75] **BCDMS** Collaboration, A. C. Benvenuti et al., *A High Statistics Measurement of the Proton Structure Functions  $F_2(x, Q^2)$  and  $R$  from Deep Inelastic Muon Scattering at High  $Q^2$* , Phys. Lett. **B223** (1989) 485.
- [76] **BCDMS** Collaboration, A. C. Benvenuti et al., *A High Statistics Measurement of the Deuteron Structure Functions  $F_2(x, Q^2)$  and  $R$  from Deep Inelastic Muon Scattering at High  $Q^2$* , Phys. Lett. **B237** (1990) 592.
- [77] **CHORUS** Collaboration, G. Onengut et al., *Measurement of nucleon structure functions in neutrino scattering*, Phys. Lett. **B632** (2006) 65–75.
- [78] **NuTeV** Collaboration, M. Goncharov et al., *Precise measurement of dimuon production cross-sections in  $\nu_\mu Fe$  and  $\bar{\nu}_\mu Fe$  deep inelastic scattering at the Tevatron*, Phys. Rev. **D64** (2001) 112006, [[hep-ex/0102049](#)].
- [79] **ZEUS, H1** Collaboration, H. Abramowicz et al., *Combination of measurements of inclusive deep inelastic  $e^\pm p$  scattering cross sections and QCD analysis of HERA data*, Eur. Phys. J. **C75** (2015), no. 12 580, [[arXiv:1506.06042](#)].
- [80] **H1, ZEUS** Collaboration, H. Abramowicz et al., *Combination and QCD analysis of charm and beauty production cross-section measurements in deep inelastic  $ep$  scattering at HERA*, Eur. Phys. J. **C78** (2018), no. 6 473, [[arXiv:1804.01019](#)].
- [81] **ATLAS** Collaboration, M. Aaboud et al., *Measurement of differential cross sections and  $W^+/W^-$  cross-section ratios for  $W$  boson production in association with jets at  $\sqrt{s} = 8$  TeV with the ATLAS detector*, JHEP **05** (2018) 077, [[arXiv:1711.03296](#)]. [Erratum: JHEP 10, 048 (2020)].
- [82] **FNAL E866/NuSea** Collaboration, R. S. Towell et al., *Improved measurement of the anti- $d$ /anti- $u$  asymmetry in the nucleon sea*, Phys. Rev. **D64** (2001) 052002, [[hep-ex/0103030](#)].
- [83] **NuSea** Collaboration, J. C. Webb et al., *Absolute Drell-Yan dimuon cross sections in 800-GeV/c  $p p$  and  $p d$  collisions*, [hep-ex/0302019](#).
- [84] G. Moreno et al., *Dimuon production in proton - copper collisions at  $\sqrt{s} = 38.8$ -GeV*, Phys. Rev. **D43** (1991) 2815–2836.
- [85] **SeaQuest** Collaboration, J. Dove et al., *The asymmetry of antimatter in the proton*, Nature **590** (2021), no. 7847 561–565, [[arXiv:2103.04024](#)].
- [86] **ATLAS** Collaboration, G. Aad et al., *Measurement of the low-mass Drell-Yan differential cross section at  $\sqrt{s} = 7$  TeV using the ATLAS detector*, JHEP **06** (2014) 112, [[arXiv:1404.1212](#)].

- [87] **ATLAS** Collaboration, G. Aad et al., *Measurement of the high-mass Drell–Yan differential cross-section in pp collisions at  $\sqrt{s}=7$  TeV with the ATLAS detector*, Phys.Lett. **B725** (2013) 223, [[arXiv:1305.4192](#)].
- [88] **ATLAS** Collaboration, G. Aad et al., *Measurement of the transverse momentum and  $\phi_\eta^*$  distributions of Drell–Yan lepton pairs in proton–proton collisions at  $\sqrt{s} = 8$  TeV with the ATLAS detector*, Eur. Phys. J. **C76** (2016), no. 5 291, [[arXiv:1512.02192](#)].
- [89] **CMS** Collaboration, V. Khachatryan et al., *Measurement of the differential cross section for top quark pair production in pp collisions at  $\sqrt{s} = 8$  TeV*, Eur. Phys. J. **C75** (2015), no. 11 542, [[arXiv:1505.04480](#)].
- [90] **CDF** Collaboration, T. A. Aaltonen et al., *Measurement of  $d\sigma/dy$  of Drell-Yan  $e^+e^-$  pairs in the Z Mass Region from  $p\bar{p}$  Collisions at  $\sqrt{s} = 1.96$  TeV*, Phys. Lett. **B692** (2010) 232–239, [[arXiv:0908.3914](#)].
- [91] **D0** Collaboration, V. M. Abazov et al., *Measurement of the shape of the boson rapidity distribution for  $p\bar{p} \rightarrow Z/\gamma^* \rightarrow e^+e^- + X$  events produced at  $\sqrt{s}=1.96$ -TeV*, Phys. Rev. **D76** (2007) 012003, [[hep-ex/0702025](#)].
- [92] **D0** Collaboration, V. M. Abazov et al., *Measurement of the muon charge asymmetry in  $p\bar{p} \rightarrow W+X \rightarrow \mu\nu + X$  events at  $\sqrt{s}=1.96$  TeV*, Phys.Rev. **D88** (2013) 091102, [[arXiv:1309.2591](#)].
- [93] **ATLAS** Collaboration, G. Aad et al., *Measurement of the inclusive  $W^\pm$  and  $Z/\gamma^*$  cross sections in the electron and muon decay channels in pp collisions at  $\sqrt{s}=7$  TeV with the ATLAS detector*, Phys.Rev. **D85** (2012) 072004, [[arXiv:1109.5141](#)].
- [94] **ATLAS** Collaboration, M. Aaboud et al., *Precision measurement and interpretation of inclusive  $W^+$ ,  $W^-$  and  $Z/\gamma^*$  production cross sections with the ATLAS detector*, Eur. Phys. J. **C77** (2017), no. 6 367, [[arXiv:1612.03016](#)].
- [95] **ATLAS** Collaboration, G. Aad et al., *Measurement of the double-differential high-mass Drell-Yan cross section in pp collisions at  $\sqrt{s} = 8$  TeV with the ATLAS detector*, JHEP **08** (2016) 009, [[arXiv:1606.01736](#)].
- [96] **ATLAS** Collaboration, M. Aaboud et al., *Measurement of the Drell-Yan triple-differential cross section in pp collisions at  $\sqrt{s} = 8$  TeV*, JHEP **12** (2017) 059, [[arXiv:1710.05167](#)].
- [97] **CMS** Collaboration, S. Chatrchyan et al., *Measurement of the electron charge asymmetry in inclusive W production in pp collisions at  $\sqrt{s} = 7$  TeV*, Phys.Rev.Lett. **109** (2012) 111806, [[arXiv:1206.2598](#)].
- [98] **CMS** Collaboration, S. Chatrchyan et al., *Measurement of the muon charge asymmetry in inclusive pp to WX production at  $\sqrt{s} = 7$  TeV and an improved determination of light parton distribution functions*, Phys.Rev. **D90** (2014) 032004, [[arXiv:1312.6283](#)].
- [99] **CMS** Collaboration, S. Chatrchyan et al., *Measurement of the differential and double-differential Drell-Yan cross sections in proton-proton collisions at  $\sqrt{s} = 7$  TeV*, JHEP **1312** (2013) 030, [[arXiv:1310.7291](#)].
- [100] **CMS** Collaboration, V. Khachatryan et al., *Measurement of the differential cross section and charge asymmetry for inclusive  $pp \rightarrow W^\pm + X$  production at  $\sqrt{s} = 8$  TeV*, Eur. Phys. J. **C76** (2016), no. 8 469, [[arXiv:1603.01803](#)].
- [101] **LHCb** Collaboration, R. Aaij et al., *Measurement of the cross-section for  $Z \rightarrow e^+e^-$  production in pp collisions at  $\sqrt{s} = 7$  TeV*, JHEP **1302** (2013) 106, [[arXiv:1212.4620](#)].

- [102] **LHCb** Collaboration, R. Aaij et al., *Measurement of forward  $Z \rightarrow e^+e^-$  production at  $\sqrt{s} = 8$  TeV*, JHEP **05** (2015) 109, [[arXiv:1503.00963](#)].
- [103] **LHCb** Collaboration, R. Aaij et al., *Measurement of the forward  $Z$  boson production cross-section in  $pp$  collisions at  $\sqrt{s} = 7$  TeV*, JHEP **08** (2015) 039, [[arXiv:1505.07024](#)].
- [104] **LHCb** Collaboration, R. Aaij et al., *Measurement of forward  $W$  and  $Z$  boson production in  $pp$  collisions at  $\sqrt{s} = 8$  TeV*, JHEP **01** (2016) 155, [[arXiv:1511.08039](#)].
- [105] **LHCb** Collaboration, R. Aaij et al., *Measurement of the forward  $Z$  boson production cross-section in  $pp$  collisions at  $\sqrt{s} = 13$  TeV*, JHEP **09** (2016) 136, [[arXiv:1607.06495](#)].
- [106] **ATLAS** Collaboration, M. Aaboud et al., *Measurement of the inclusive jet cross-sections in proton-proton collisions at  $\sqrt{s} = 8$  TeV with the ATLAS detector*, JHEP **09** (2017) 020, [[arXiv:1706.03192](#)].
- [107] **CMS** Collaboration, V. Khachatryan et al., *Measurement and QCD analysis of double-differential inclusive jet cross sections in  $pp$  collisions at  $\sqrt{s} = 8$  TeV and cross section ratios to 2.76 and 7 TeV*, JHEP **03** (2017) 156, [[arXiv:1609.05331](#)].
- [108] **ATLAS Collaboration** Collaboration, G. Aad et al., *Measurement of dijet cross sections in  $pp$  collisions at 7 TeV centre-of-mass energy using the ATLAS detector*, JHEP **1405** (2014) 059, [[arXiv:1312.3524](#)].
- [109] **CMS** Collaboration, S. Chatrchyan et al., *Measurements of differential jet cross sections in proton-proton collisions at  $\sqrt{s} = 7$  TeV with the CMS detector*, Phys.Rev. **D87** (2013) 112002, [[arXiv:1212.6660](#)].
- [110] **ATLAS** Collaboration, M. Aaboud et al., *Measurement of the cross section for inclusive isolated-photon production in  $pp$  collisions at  $\sqrt{s} = 13$  TeV using the ATLAS detector*, Phys. Lett. B **770** (2017) 473–493, [[arXiv:1701.06882](#)].
- [111] **ATLAS** Collaboration, M. Aaboud et al., *Measurement of top quark pair differential cross-sections in the dilepton channel in  $pp$  collisions at  $\sqrt{s} = 7$  and 8 TeV with ATLAS*, Phys. Rev. D **94** (2016), no. 9 092003, [[arXiv:1607.07281](#)]. [Addendum: Phys.Rev.D 101, 119901 (2020)].
- [112] **ATLAS** Collaboration, G. Aad et al., *Measurements of top-quark pair differential and double-differential cross-sections in the  $\ell$ +jets channel with  $pp$  collisions at  $\sqrt{s} = 13$  TeV using the ATLAS detector*, Eur. Phys. J. C **79** (2019), no. 12 1028, [[arXiv:1908.07305](#)]. [Erratum: Eur.Phys.J.C 80, 1092 (2020)].
- [113] **CMS** Collaboration, A. M. Sirunyan et al., *Measurements of  $t\bar{t}$  differential cross sections in proton-proton collisions at  $\sqrt{s} = 13$  TeV using events containing two leptons*, JHEP **02** (2019) 149, [[arXiv:1811.06625](#)].
- [114] **CMS** Collaboration, A. Tumasyan et al., *Measurement of differential  $t\bar{t}$  production cross sections in the full kinematic range using lepton+jets events from proton-proton collisions at  $\sqrt{s} = 13$  TeV*, [arXiv:2108.02803](#).
- [115] **ATLAS** Collaboration, G. Aad et al., *Measurements of the charge asymmetry in top-quark pair production in the dilepton final state at  $\sqrt{s} = 8$  TeV with the ATLAS detector*, Phys. Rev. D **94** (2016), no. 3 032006, [[arXiv:1604.05538](#)].
- [116] **ATLAS** Collaboration, A. collaboration, *Evidence for the charge asymmetry in  $pp \rightarrow t\bar{t}$  production at  $\sqrt{s} = 13$  TeV with the ATLAS detector*, [arXiv:2208.12095](#).

- [117] **CMS Collaboration**, V. Khachatryan et al., *Measurements of  $t\bar{t}$  charge asymmetry using dilepton final states in  $pp$  collisions at  $\sqrt{s} = 8$  TeV*, Phys. Lett. B **760** (2016) 365–386, [[arXiv:1603.06221](#)].
- [118] **CMS Collaboration** Collaboration, C. collaboration, *Measurement of the  $t\bar{t}$  charge asymmetry in highly boosted events in the single-lepton channel at 13 TeV*, tech. rep., CERN, Geneva, 2022.
- [119] **ATLAS, CMS Collaboration**, M. Aaboud et al., *Combination of inclusive and differential  $t\bar{t}$  charge asymmetry measurements using ATLAS and CMS data at  $\sqrt{s} = 7$  and 8 TeV*, JHEP **04** (2018) 033, [[arXiv:1709.05327](#)].
- [120] **ATLAS Collaboration**, G. Aad et al., *Measurements of the inclusive and differential production cross sections of a top-quark-antiquark pair in association with a Z boson at  $\sqrt{s} = 13$  TeV with the ATLAS detector*, Eur. Phys. J. C **81** (2021), no. 8 737, [[arXiv:2103.12603](#)].
- [121] CMS Collaboration, *Measurement of top quark pair production in association with a z boson in proton-proton collisions at  $\sqrt{s} = 13$  TeV*, [arXiv:1907.11270](#).
- [122] **ATLAS Collaboration**, G. Aad et al., *Comprehensive measurements of  $t$ -channel single top-quark production cross sections at  $\sqrt{s} = 7$  TeV with the ATLAS detector*, Phys. Rev. D **90** (2014), no. 11 112006, [[arXiv:1406.7844](#)].
- [123] **ATLAS Collaboration**, M. Aaboud et al., *Fiducial, total and differential cross-section measurements of  $t$ -channel single top-quark production in  $pp$  collisions at 8 TeV using data collected by the ATLAS detector*, Eur. Phys. J. C **77** (2017), no. 8 531, [[arXiv:1702.02859](#)].
- [124] **CMS Collaboration**, A. M. Sirunyan et al., *Measurement of differential cross sections and charge ratios for  $t$ -channel single top quark production in proton-proton collisions at  $\sqrt{s} = 13$  TeV*, Eur. Phys. J. C **80** (2020), no. 5 370, [[arXiv:1907.08330](#)].
- [125] **ATLAS Collaboration**, G. Aad et al., *Measurements of top-quark pair differential cross-sections in the lepton+jets channel in  $pp$  collisions at  $\sqrt{s} = 8$  TeV using the ATLAS detector*, Eur. Phys. J. C **76** (2016), no. 10 538, [[arXiv:1511.04716](#)].
- [126] **ATLAS Collaboration**, G. Aad et al., *Measurements of top-quark pair single- and double-differential cross-sections in the all-hadronic channel in  $pp$  collisions at  $\sqrt{s} = 13$  TeV using the ATLAS detector*, JHEP **01** (2021) 033, [[arXiv:2006.09274](#)].
- [127] **CMS Collaboration**, A. M. Sirunyan et al., *Measurement of double-differential cross sections for top quark pair production in  $pp$  collisions at  $\sqrt{s} = 8$  TeV and impact on parton distribution functions*, Eur. Phys. J. C **77** (2017), no. 7 459, [[arXiv:1703.01630](#)].
- [128] **ATLAS Collaboration**, G. Aad et al., *Measurement of  $W^\pm$  and Z-boson production cross sections in  $pp$  collisions at  $\sqrt{s} = 13$  TeV with the ATLAS detector*, Phys. Lett. B **759** (2016) 601–621, [[arXiv:1603.09222](#)].
- [129] **ATLAS Collaboration**, G. Aad et al., *Measurement of the  $t\bar{t}$  production cross-section using  $e\mu$  events with  $b$ -tagged jets in  $pp$  collisions at  $\sqrt{s} = 7$  and 8 TeV with the ATLAS detector*, Eur. Phys. J. C **74** (2014), no. 10 3109, [[arXiv:1406.5375](#)]. [Addendum: Eur. Phys. J. C **76**, no. 11, 642 (2016)].
- [130] **ATLAS Collaboration**, M. Aaboud et al., *Measurement of the inclusive and fiducial  $t\bar{t}$  production cross-sections in the lepton+jets channel in  $pp$  collisions at  $\sqrt{s} = 8$  TeV with the ATLAS detector*, Eur. Phys. J. C **78** (2018) 487, [[arXiv:1712.06857](#)].

- [131] **ATLAS** Collaboration, G. Aad et al., *Measurement of the  $t\bar{t}$  production cross-section and lepton differential distributions in  $e\mu$  dilepton events from  $pp$  collisions at  $\sqrt{s} = 13$  TeV with the ATLAS detector*, Eur. Phys. J. C **80** (2020), no. 6 528, [[arXiv:1910.08819](#)].
- [132] **ATLAS** Collaboration, G. Aad et al., *Measurement of the  $t\bar{t}$  production cross-section in the lepton+jets channel at  $\sqrt{s} = 13$  TeV with the ATLAS experiment*, Phys. Lett. B **810** (2020) 135797, [[arXiv:2006.13076](#)].
- [133] **CMS** Collaboration, A. M. Sirunyan et al., *Measurement of the inclusive  $t\bar{t}$  cross section in  $pp$  collisions at  $\sqrt{s} = 5.02$  TeV using final states with at least one charged lepton*, JHEP **03** (2018) 115, [[arXiv:1711.03143](#)].
- [134] S. Spannagel, *Top quark mass measurements with the CMS experiment at the LHC*, PoS **DIS2016** (2016) 150, [[arXiv:1607.04972](#)].
- [135] **CMS** Collaboration, V. Khachatryan et al., *Measurement of the top quark pair production cross section in proton-proton collisions at  $\sqrt{s} = 13$  TeV*, Phys. Rev. Lett. **116** (2016), no. 5 052002, [[arXiv:1510.05302](#)].
- [136] **ATLAS** Collaboration, G. Aad et al., *Measurement of the  $t\bar{t}W$  and  $t\bar{t}Z$  production cross sections in  $pp$  collisions at  $\sqrt{s} = 8$  TeV with the ATLAS detector*, JHEP **11** (2015) 172, [[arXiv:1509.05276](#)].
- [137] **ATLAS** Collaboration, M. Aaboud et al., *Measurement of the  $t\bar{t}Z$  and  $t\bar{t}W$  cross sections in proton-proton collisions at  $\sqrt{s} = 13$  TeV with the ATLAS detector*, Phys. Rev. D **99** (2019), no. 7 072009, [[arXiv:1901.03584](#)].
- [138] **CMS** Collaboration, V. Khachatryan et al., *Observation of top quark pairs produced in association with a vector boson in  $pp$  collisions at  $\sqrt{s} = 8$  TeV*, JHEP **01** (2016) 096, [[arXiv:1510.01131](#)].
- [139] **CMS** Collaboration, A. M. Sirunyan et al., *Measurement of the cross section for top quark pair production in association with a  $W$  or  $Z$  boson in proton-proton collisions at  $\sqrt{s} = 13$  TeV*, JHEP **08** (2018) 011, [[arXiv:1711.02547](#)].
- [140] **ATLAS** Collaboration, G. Aad et al., *Evidence for single top-quark production in the  $s$ -channel in proton-proton collisions at  $\sqrt{s} = 8$  TeV with the ATLAS detector using the Matrix Element Method*, Phys. Lett. B **756** (2016) 228–246, [[arXiv:1511.05980](#)].
- [141] **ATLAS** Collaboration, M. Aaboud et al., *Measurement of the inclusive cross-sections of single top-quark and top-antiquark  $t$ -channel production in  $pp$  collisions at  $\sqrt{s} = 13$  TeV with the ATLAS detector*, JHEP **04** (2017) 086, [[arXiv:1609.03920](#)].
- [142] **ATLAS** Collaboration, A. collaboration, *Measurement of single top-quark production in the  $s$ -channel in proton–proton collisions at  $\sqrt{s} = 13$  TeV with the ATLAS detector*, [arXiv:2209.08990](#).
- [143] **CMS** Collaboration, S. Chatrchyan et al., *Measurement of the Single-Top-Quark  $t$ -Channel Cross Section in  $pp$  Collisions at  $\sqrt{s} = 7$  TeV*, JHEP **12** (2012) 035, [[arXiv:1209.4533](#)].
- [144] **CMS** Collaboration, V. Khachatryan et al., *Measurement of the  $t$ -channel single-top-quark production cross section and of the  $|V_{tb}|$  CKM matrix element in  $pp$  collisions at  $\sqrt{s} = 8$  TeV*, JHEP **06** (2014) 090, [[arXiv:1403.7366](#)].
- [145] **CMS** Collaboration, V. Khachatryan et al., *Search for  $s$  channel single top quark production in  $pp$  collisions at  $\sqrt{s} = 7$  and 8 TeV*, JHEP **09** (2016) 027, [[arXiv:1603.02555](#)].

- [146] **CMS** Collaboration, A. M. Sirunyan et al., *Cross section measurement of  $t$ -channel single top quark production in  $pp$  collisions at  $\sqrt{s} = 13$  TeV*, Phys. Lett. B **772** (2017) 752–776, [[arXiv:1610.00678](#)].
- [147] **ATLAS** Collaboration, G. Aad et al., *Measurement of the production cross-section of a single top quark in association with a  $W$  boson at 8 TeV with the ATLAS experiment*, JHEP **01** (2016) 064, [[arXiv:1510.03752](#)].
- [148] **ATLAS** Collaboration, G. Aad et al., *Measurement of single top-quark production in association with a  $W$  boson in the single-lepton channel at  $\sqrt{s} = 8$  TeV with the ATLAS detector*, Eur. Phys. J. C **81** (2021), no. 8 720, [[arXiv:2007.01554](#)].
- [149] **ATLAS** Collaboration, M. Aaboud et al., *Measurement of the cross-section for producing a  $W$  boson in association with a single top quark in  $pp$  collisions at  $\sqrt{s} = 13$  TeV with ATLAS*, JHEP **01** (2018) 063, [[arXiv:1612.07231](#)].
- [150] **CMS** Collaboration, S. Chatrchyan et al., *Observation of the associated production of a single top quark and a  $W$  boson in  $pp$  collisions at  $\sqrt{s} = 8$  TeV*, Phys. Rev. Lett. **112** (2014), no. 23 231802, [[arXiv:1401.2942](#)].
- [151] **CMS** Collaboration, A. M. Sirunyan et al., *Measurement of the production cross section for single top quarks in association with  $W$  bosons in proton-proton collisions at  $\sqrt{s} = 13$  TeV*, JHEP **10** (2018) 117, [[arXiv:1805.07399](#)].
- [152] **CMS** Collaboration, A. Tumasyan et al., *Observation of  $tW$  production in the single-lepton channel in  $pp$  collisions at  $\sqrt{s} = 13$  TeV*, JHEP **11** (2021) 111, [[arXiv:2109.01706](#)].